

1 **Assessing the Sources of Submicron Airborne Elements at two sites in** 2 **the Fos-Marseille Basin through Rolling Positive Matrix Factorization**

3 Mathilde Brezins¹, Benjamin Chazeau¹, Nicolas Marchand¹, Amandine Durand¹, Grégory Gille², Romain
4 Bourjot², Andre S.H. Prévôt³, Jean-Luc Jaffrezo⁴, Gaëlle Uzu⁴ and Barbara D'Anna¹

5 ¹Aix Marseille Univ, CNRS, LCE, Marseille, 13331, France

6 ²AtmoSud, Regional Network for Air Quality Monitoring of Provence-Alpes-Côte-d'Azur, Marseille, France

7 ³Laboratory of Atmospheric Chemistry, Paul Scherrer Institute, 5232 Villigen, Switzerland

8 ⁴Univ. Grenoble Alpes, CNRS, IRD, INP, IGE (UMR 5001), 38000 Grenoble, France

9
10 *Correspondence to:* Benjamin Chazeau (benjamin.chazeau@univ-amu.fr), Barbara D'Anna (barbara.danna@univ-amu.fr)

11 **Abstract.**

12
13 Contributions and evolution of fine elemental particulate matter (PM) sources were investigated in the Marseille-Fos basin
14 (South of France) based on a 1 year-long (January-December 2023) study using on-line x-ray fluorescence (Xact) PM₁
15 measurements. The region's intense anthropogenic activity and complex meteorological conditions make it an ideal case study
16 for fine aerosol characterization. Given the limited information available on fine elemental sources in the area, a dual-site
17 approach was implemented, combining an urban background site (MRS-LCP) and an industrial site (FOS) to distinguish
18 between regional and local emission influences. Source apportionment was conducted using a rolling Positive Matrix
19 Factorization (PMF) method, implemented via the Source Finder Professional (SoFi) toolkit. Several tests were carried out to
20 determine optimal rolling PMF parameters. Eventually, a 21-day rolling window configuration was selected, resolving nine
21 factors at FOS and eight at MRS-LCP, with seven similar factors detected at both sites. Among them, three were attributed to
22 secondary aerosols, including sulfur photooxidation leading to sulfate-rich aerosols (S-rich factor) and the formation of
23 halogenated reactive particulate species (Cl-rich and Br-rich factors). Additionally, biomass burning, shipping, and dust related
24 factors were identified at both locations. In contrast, three industrial factors (Steel Industry, Zn-Industrial, Pb-Industrial) were
25 detected at FOS, while only the Steel Industry factor appeared at MRS-LCP, suggesting downwind transport of industrial
26 plumes from Fos-sur-Mer to Marseille under Mistral and thermal breeze regimes. Furthermore, the comparison of dynamic
27 rolling PMF approach to static PMF analysis, demonstrated higher dissimilarities across factors profiles, reflecting enhanced
28 ability of Rolling PMF to capture seasonal variability in aerosol sources. Overall, this study highlights the dominant
29 anthropogenic imprint on submicron PM elements and the effectiveness of dynamic source apportionment in complex coastal-
30 industrial environments.

31 **1 Introduction**

32 Air pollution has long been recognized as a major threat to human health (Dockery et al., 1993), representing the leading
33 environmental risk factor for premature mortality globally and the second leading overall risk factor for death (WHO, 2021).
34 Fuller et al. (2022) estimated it was responsible for 9 million premature deaths per year worldwide. Intensified anthropogenic
35 activities, particularly urbanization, industrialization, and widespread fossil fuel use, further degrade air quality, presenting a
36 double jeopardy as they impact both human health and the climate system (Schmale et al., 2014). In a context of rapid climate
37 change, understanding the complex interplay of aerosols is crucial, as climate change may further increase aerosol production
38 (e.g., more frequent Saharan dust outbreaks, increased wildfire episodes, and volatile organic compound emissions from
39 stressed vegetation) (Gomez et al., 2022; Bourtsoukidis et al., 2024; Pons et al., 2025). Climate change hot spots such as the
40 Mediterranean Basin are particularly at risk, with projections indicating more frequent and intense meteorological extremes
41 that could trigger additional pollution episodes (Zittis et al., 2022; Jézéquel et al., 2025).

42 The city of Marseille (France) embodies these vulnerabilities. With its dense population and exposure to numerous pollution
43 sources, it represents a highly complex and dynamic atmospheric environment. Anthropogenic activities in the region include
44 one of the largest ports in the Mediterranean Sea, and major industrial facilities. In particular, industrial sites located in the
45 north-western suburbs of the Marseille-Fos basin are recognized contributors to Marseille's air pollution (El Haddad et al.,
46 2013; Salameh et al., 2018; Chazeau et al., 2021). The diversity of pollution sources, combined with local meteorological
47 conditions, such as frequent land-sea breeze circulations, favour the ageing and formation of secondary aerosols (Puygrenier
48 et al., 2005; Drobinski et al., 2007), effectively transforming the Marseille basin into a chemical reactor for atmospheric
49 particles. This complexity has drawn significant scientific attention to the region (Bozetti et al., 2017; Chevet et al., 2024;
50 Dufresne et al., 2025). In particular, fine particulate matter smaller than 1 μm (PM_{10}) is a major health concern, due to its ability
51 to penetrate deeply into the respiratory system (Kreyling et al., 2006), but it remains unregulated in France. Consequently,
52 submicron aerosol composition and dynamics in the Marseille area have attracted growing scientific interest in recent years
53 (El Haddad et al., 2013; Chazeau et al., 2021; Camman et al., 2024; Le Berre et al., 2025).

54 While several studies have characterized the organic fraction of submicron aerosols in Marseille (Haddad et al., 2013; Bozetti
55 et al., 2017; Chazeau et al., 2022), source apportionment of airborne elements, including non-metals, metals and metalloids,
56 remains scarce (Camman et al., 2024). This is critical, as many metallic elements such as Pb, Hg, As, Cr, Ni, and Cd are found
57 to be toxic, bioaccumulative, and associated with carcinogenic, neurotoxic, or cardiovascular effects (Rose, 1983). Recent
58 advances in automated, high-time-resolution energy-dispersive X-ray fluorescence (ED-XRF) instrumentation (e.g., Xact 625i,
59 Cooper Environmental Services) allow continuous, highly-time resolved measurements of a wide range of airborne elements
60 (Furger et al., 2017; Tremper et al., 2018), offering new opportunities to assess airborne elements source dynamics and
61 temporal variability.

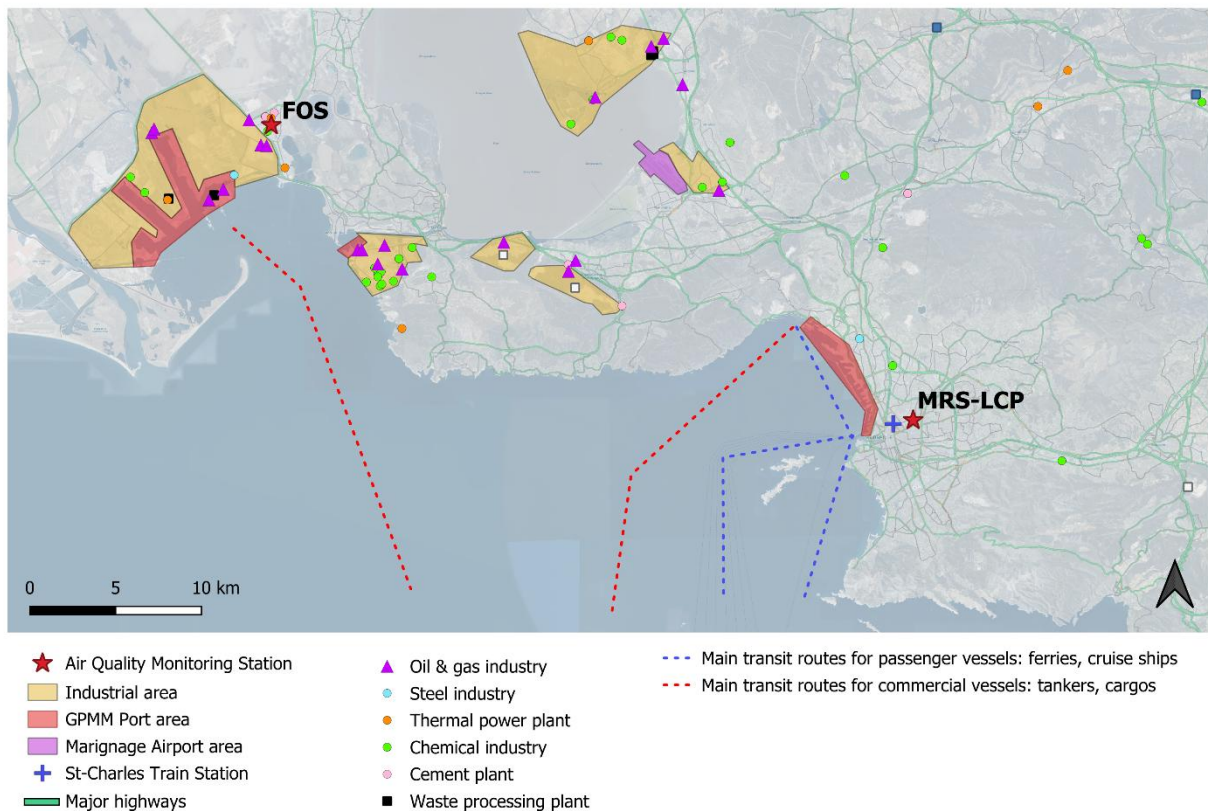
62 In this study, we aim to identify and characterize the sources of submicron airborne elements in the Marseille-Fos basin using
63 the whole 2023 year of high-time resolution Xact measurement data. To capture temporal variability in source profiles and

64 contributions, we apply Rolling Positive Matrix Factorization (Rolling PMF), a dynamic source apportionment approach
65 recently introduced by Canonaco et al. (2021). This method improves upon conventional static PMF by capturing short-term
66 seasonal variations in factor profiles. Although Rolling PMF has been widely used for AMS/ACSM datasets (Heikkinen et al.,
67 2021; Tobler et al., 2021; Chen et al., 2021, 2022a, 2022b; Lin et al., 2022; Via et al., 2022; Chazeau et al., 2022; Chebaicheb
68 et al., 2023; Lei et al., 2025), its application to Xact data remains limited (Manousakas et al., 2025) and no application of
69 Rolling PMF methodology upon 1 year-long Xact data has been reported yet. This is particularly important because several
70 non-metal elements measured by the Xact (e.g., S, Se, Cl, Br) can undergo rapid atmospheric transformations, which static
71 PMF approaches may fail to capture.

72 **2 Instrument & Methods**

73 **2.1 Dual-Site Description**

74 The Marseille-Fos basin is a semi-enclosed coastal basin in the northwestern Mediterranean, covering nearly 2500 km² and
75 including the Gulf of Fos-sur-Mer and the Bay of Marseille, the second most populated city in France. The region experiences
76 intensive anthropogenic pressure due to major industrial, urban, and maritime activities (Fig. 1). The Berre Pond industrial
77 area is one of the largest in France, encompassing steel manufacturing plants, oil refineries, petrochemical facilities, cement
78 factories, and stone quarries, and the Fos-sur-Mer incinerator. Additionally, a major thermal power plant, the Gardanne facility,
79 is located 20 km north-east of Marseille's city centre (Fig. 1). In parallel, the Grand Port Maritime de Marseille (GPMM), the
80 second-largest port in France, extends from Fos-sur-Mer to the northern part of Marseille. In 2023, the GPMM processed over
81 72 million tonnes of goods and welcomed more than 4 million cruise passengers (<https://www.marseille-port.fr>). It comprises
82 the Fos industrial harbour (between Port-Saint-Louis and Fos-sur-Mer) and the Port-de-Bouc terminal at the entrance of the
83 Berre Channel. Together, these facilities delimit the Gulf of Fos, forming the largest industrial-port complex in France. On the
84 other side of the basin, previous studies have demonstrated that maritime traffic in the Bay of Marseille, including emissions
85 from vessels at berth, contributes significantly to urban air pollution levels (Chazeau et al., 2021; Le Berre et al., 2025).
86 Additionally, Marseille is characterized by intense vehicular activity as the city hosts the second largest car fleet in France
87 (Bilan Annuel des Transports 2023, <https://www.statistiques.developpement-durable.gouv.fr/>).



88

89 **Figure 1: Map of the Marseille–Fos basin. Locations of industrial plants were obtained from the SEVESO and IREP databases**
 90 **(<https://data.ampmetropole.fr/>). Main ship transit routes were derived from MarineTraffic**
 91 **(<https://www.marinetraffic.com/>). Major highways were sourced from Google Traffic**
 92 **(©Google). Background map layers were provided by Carto Positron and Bing Satellite. The map was produced using QGIS 3.34.**

93 The combination of such diverse anthropogenic activities generates a complex mixture of primary pollutants, which undergo
 94 chemical transformation and are transported across the Marseille-Fos basin. The region is characterized by high solar radiation
 95 during summer, promoting photochemical activity, including ozone formation and secondary organic aerosol (SOA)
 96 production (El Haddad et al., 2013; Chazeau et al., 2021). Prevailing wind regimes in the Marseille-Fos basin are dominated
 97 by the Mistral and thermal breezes, both playing a major role in pollutant transport. The Mistral, a synoptic northwesterly wind
 98 (270° - 360°) channeled through the Rhône Valley, would be expected to affect both sites similarly; however, it was reported
 99 54 % of the time at Fos-sur-Mer and 35 % at Marseille in 2023, likely reflecting local shielding effects from surrounding hills
 100 and vegetation. Thermal breezes were observed approximately 40% of the time in the Marseille-Fos basin. These are
 101 characterized by nocturnal land breezes (5° - 90°) and daytime sea breezes (210° - 270° in Marseille; 120° - 240° in Fos-sur-Mer).
 102 In addition, the region is occasionally impacted by strong southeasterly Sirocco winds, which transport Saharan dust across
 103 the Mediterranean (Flaounas et al., 2009). In 2023, six dust episodes, lasting from 1 to 4 days, were recorded. The basin’s
 104 complex topography further modulates atmospheric transport. Marseille is also bordered by mountainous terrain, with the

105 Massif de l'Étoile to the north (778 m a.s.l.) and the Calanques massifs to the south (646 m a.s.l.). The combination of complex
106 terrain and variable meteorological conditions results in substantial variability in the Boundary Layer Height (BLH), ranging
107 from over 1000 m during summer Mistral events to below 500 m under wintertime thermal breeze conditions (Riandet et al.,
108 2023), thus affecting aerosol dispersion and dilution.

109 To investigate the atmospheric composition in this complex environment, data from two air quality monitoring supersites were
110 used, both operated by the Laboratory of Environmental Chemistry (LCE) and AtmoSud (<https://www.atmosud.org>). The first
111 one, the Marseille-Longchamp Observatory supersite (MRS-LCP), is located in the center of Marseille, in Longchamp Park
112 near the Marseille Observatory (43°18'18.84'' N; 5°23'40.89'' E; 71 m a.s.l.). Continuously operating for nearly two decades,
113 this station is classified as an urban background site according to European Environment Agency criteria (Larssen et al., 1999).
114 Positioned approximately 3 km inland from the Mediterranean coastline and within the city center, it is representative of typical
115 coastal urban air quality conditions. MRS-LCP has been featured in multiple studies (El Haddad et al., 2011; Salameh et al.,
116 2018; Chazeau et al., 2021; Camman et al., 2024) and has been recently selected as a French urban super site for the new EU
117 regulation. The second site, the Fos-Carabins Monitoring Station (FOS, 43°27'32.092'' N; 4°56'4.412'' E; 5 m a.s.l.), is
118 located in the residential area of Fos Les Carabins but is classified as periurban site under industrial influence due to its
119 proximity to the port-industrial complex of Fos-sur-Mer and its exposure to emissions from surrounding industrial facilities,
120 including the ones of Fos-sur-Mer (< 1km southwest), and Port-de-Bouc (approximately 10 km southeast, Fig. 1). Like MRS-
121 LCP, the FOS station is located approximately 3 km from the coastline. Despite being 40 km apart, meteorological conditions
122 enable the transport of aerosol between both sites from several emissions sources. Specifically, sea-breeze events frequently
123 carry industrial plumes inland toward Marseille (Puygrenier et al., 2005; El Haddad et al., 2013), while low Mistral flows may
124 facilitate downwind transport of pollutants from the Fos-sur-Mer industrial area toward the urban center. Therefore, both
125 monitoring sites are strategically positioned to assess intra-basin transport and the interplay between urban and industrial
126 sources.

127

128 **2.2 Sampling and Instrumentation**

129 Submicronic aerosols were continuously sampled from January 1st, 2023, to December 31st, 2023, as part of the SHIPAIR
130 (“SHIPping emission’s contribution to AIRpollution in urban harbour area”) campaign (<https://anr.fr/Project-ANR-21-CE22-0015>) at both sites. Each sampling station was equipped with a range of analytical instruments for aerosol and gases monitoring,
131 as detailed in Table 1.

133

Instrument	Species	Fraction	Temporal Resolution	Technology	MRS-LCP	FOS
------------	---------	----------	---------------------	------------	---------	-----

Xact 625i <i>Cooper Environmental</i>	Trace elements	PM ₁	1h	X-Ray fluorescence (XRF)	X	X
Tof-ACSM <i>Aerodyne Research</i>	Non-refractory aerosol	PM ₁	10 min	Electron Ionisation and Time-Of-Flight Mass Spectrometry	X	
AE33 <i>Aerosol Magee Scientific</i>	Black carbon	PM _{2,5}	1 min	Spectroscopy	X	X
SMPS 3031 <i>TSI</i>	Particles number and Granulometry	15 nm - 723 nm	5 min	Electric field isolation and optical counting	X	
FIDAS 200 <i>PALAS</i>	Mass concentration	180nm – 20µm	15 min	Optical light scattering	X	
M200E <i>Teledyne API</i>	NO _x	Gas	15 min	Chemiluminescence	X	
M100 E <i>Teledyne API</i>	SO ₂	Gas	15 min	UV Fluorescence	X	X
Serinus 10 <i>Ecotech</i>	O ₃	Gas	15 min	UV Spectroscopy	X	
VOC72M Envea	BTEX, cyclohexane, Cl-Volatile Organic Compounds (Cl- VOCs): 1,2- dichloroethyl, trichloroethyl, tetrachloroethyl	Gas	1h	Gas Chromatography and photo-ionisation detector		X

134 **Table 1: Overview of the instruments deployed during the field campaign at MRS-LCP and FOS monitoring stations. “X” indicate**
135 **that the instrument was equipped at this site.**

136

137 At both sites, aerosols for elemental analysis were continuously and automatically sampled using a PM₁₀ inlet (Tisch
138 environmental, Cleves, OH, USA) coupled with a PM₁ impactor, operating at a flow rate of 16.7 L·min⁻¹. Airborne elements
139 were quantified by energy-dispersive X-ray fluorescence (ED-XRF) using the Xact 625i analyzer (Cooper Environmental
140 Services, Edgartown, MA, USA). Briefly, Particulate matter (PM) was collected onto a Teflon filter tape (PTFE membrane,
141 2µm thickness, Cooper Environmental Services). Then, incident X-rays from the tube excite the inner-shell electrons of the

142 sampled particles, generating element-specific secondary X-rays detected by a solid-state fluorescence detector. This enables
143 both identification and quantification of elements (Currie, 1977; Furger et al., 2017).

144 The instrument is designed to simultaneously quantify up to 45 elements, from Al to Bi (Xact 625i Manual, Cooper
145 Environmental Services, Table S1). For MRS-LCP and FOS, 33 elements (Fig. S1) and 27 elements (Fig. S2), respectively,
146 were individually calibrated using pure element standards provided by the manufacturer.

147 The Xact 625i enables online sampling and analysis of airborne elements over extended monitoring periods (several months)
148 at high temporal resolution. The sampling and analysis cycle ranges from 5 to 240 minutes. However, to allow for reasonable
149 Minimum Detection Limits (MDLs), a 60-minute sampling and analysis cycle was selected for this campaign.

150 Nevertheless, there are some limitations to the use of the instrument. First, MDLs reported for the Xact 625i are generally
151 higher than those obtained with offline elemental aerosol analysis methodologies (XRF or inductively coupled plasma mass
152 spectrometry, ICP-MS) (Tremper et al., 2018; Cadeo et al., 2025). Moreover, due to the self-absorption effect for low energy
153 X-rays emitted by lighter elements ($Z < 15$) (Formenti et al., 2010), the Xact 625i cannot detect elements such as Na or Mg,
154 while other elements such as Al or Si show higher MDLs (Table S1). Comparatively, synchrotron radiation-induced (SR) XRF
155 and ICP-MS techniques allow the detection of a larger range of elements (SR-XRF: $Z > 11$; ICP-MS: Na, Mg) (Visser et al.,
156 2015a; Furger et al., 2017). The lack of quantitative assessment of Na and Mg causes strong limitations for coastal sites like
157 ours where these elements provide key information on marine aerosols (e.g. fresh and aged sea salt; Pey et al., 2013a).

158 Other ancillary continuous monitoring of regulated pollutants were conducted exclusively at the MRS-LCP. Mass
159 concentrations of PM_1 , $PM_{2.5}$ and PM_{10} were measured using a FIDAS 200 optical particle counter (PALAS, Germany). Data
160 were recorded at 15-minute resolution throughout the entire measurement period. In parallel, NO_x (M200E, Teledyne API,
161 California, USA) and SO_2 (M100E, Teledyne API, California, USA) were also measured continuously with the same 15-
162 minute time resolution, with additional SO_2 monitoring using the same technique at FOS. Non-refractory (NR) PM_1 were
163 sampled using Time-of-Flight Aerosol Chemical Speciation Monitor (ToF-ACSM, Aerodyne Research Inc., USA; Fröhlich et
164 al., 2013) for the determination of organic aerosol (OA), NH_4^+ , NO_3^- , SO_4^{2-} , and Cl^- concentrations. During the whole year,
165 data were acquired and compiled at 10-minute time resolution through Igor-DAQ software, Tofware (Tofwerk, Thun,
166 Switzerland). Particle number size distributions (PNSD) in the submicron range were measured at MRS-LCP only, using
167 Scanning Mobility Particle Sizers (SMPS) with an Ultrafine Particle Counter model 3938 (TSI Inc., Minnesota, USA, CPC
168 3752, classifier 3082) providing particle counts from 15 to 723 nm every 5 min in 55 size bins.

169 Black carbon (BC) analysis was carried out at both sites with aethalometer AE33 (Magee Scientific, CA, USA) operated with
170 a $PM_{2.5}$ inlet. The dual-spot sampling method (Drinovec et al., 2015) was used to correct for filter-loading artifacts (Lack et
171 al., 2014). BC was further apportioned into BC liquid fuel (BC_{LF}) and BC solid fuel (BC_{SF}) components using the Aethalometer
172 model (Sandradewi et al., 2008b; Chazeau et al., 2021).

173 Volatile organic compounds (VOCs) including cyclohexane, 1,2-dichloroethane, trichloroethene, tetrachloroethene, and
174 BTEX (benzene, toluene, ethylbenzene, and o-, m-, and p-xylenes) were measured hourly at the FOS site using a VOC72M
175 gas chromatograph equipped with a photo-ionisation detector (Envea, France).

176 Meteorological data, including temperature, wind direction and wind speed, were recorded at both sites with an Ultrasonic 3D
177 anemometer USA-1 (METEK, Germany). Shortwave radiation and boundary layer height (BLH) for the Marseille-Fos area
178 during 2023 were retrieved from the Open-Meteo meteorological database (<https://open-meteo.com/>). Both stations were
179 connected to automated data platforms (e.g. the eSAM system, Envea), enabling daily automated quality control and
180 continuous data recording. Instruments and annual datasets visualization from both stations is accessible through the HERMES
181 platform (HERald of the MEasurement Stations, <https://hermes-aq.com/>).
182

183 **2.3 Source Apportionment methodology**

184 Detailed information on the source apportionment methodology is provided in Supplement S1: PMF methodology. Briefly,
185 Positive Matrix Factorization (PMF) is a bilinear receptor model that decomposes a chemical matrix into factor time series
186 and profiles, which can then be interpreted as emission sources (Paatero & Tapper, 1994). Unlike Principal Component
187 Analysis (PCA) or Chemical Mass balance (CMB), PMF imposes non-negativity and requires little a priori information,
188 making it particularly suited for environmental applications. The model iteratively minimises the weighted residuals (Q), with
189 “robust” mode applied to downweight outliers (Paatero, 1997). Rotational ambiguity is addressed using the ME-2 solver,
190 where the a-value approach constrains selected factors within predefined variability ranges (Paatero & Hopke, 2009). Finally,
191 the bootstrap resampling method (Efron, 1979; Ulbrich et al., 2009) provides statistical uncertainty estimates by testing the
192 stability of factors across perturbed datasets.

193 Yet, a stable statistical solution does not guarantee environmental meaning. For long-term datasets, covering several months
194 to a full year, PMF factor profiles may exhibit seasonal variability that is not captured by the static PMF method. To address
195 this, Parworth et al. (2015) introduced the Rolling PMF approach, which applies PMF in a rolling window to capture temporal
196 variability in factors. This method allows for the identification of short-term source behaviour that would otherwise be
197 averaged out in static analyses and has been shown to provide more environmentally interpretable results than conventional
198 static PMF, especially in capturing short-term and seasonal atmospheric events (Lin et al., 2022; Guo et al., 2025). In this
199 study, both static and rolling PMF analyses were applied to hourly trace element data, at both the urban MRS-LCP and
200 industrial FOS sites. Analyses were conducted using the SoFi Pro (Source Finder) toolkit (Datalystica Ltd., Villigen,
201 Switzerland, Canonaco et al., 2013; 2021), an Igor Pro based program (WaveMetrics, Inc., Portland, OR, USA).

202 PMF results from both static and rolling approaches were compared in terms of their ability to capture temporal variability of
203 sources, by analyzing the dissimilarity of the factor profiles using Pearson Distance and Standardized Identity Distance (PD-
204 SID) analysis (S2: PD-SID; Belis et al., 2015; Pernigotti & Belis, 2018). While PD-SID has been widely used to assess factor
205 homogeneity across multiple sites (Weber et al., 2019; Borlaza et al., 2021; Manousakas et al., 2022; Liu et al., 2025), few
206 studies have reported its use for evaluating factor homogeneity at a single site (Ngoc Thuy et al., 2025). Additionally, cosine
207 similarity, commonly employed to calculate correlations between mass spectra (Stein & Scott, 1994; Ulbrich et al., 2009), was

208 adapted to elemental factor compositions (Cosine Distance, CD, S3: Cosine Distance) to assess the variability of PMF factor
209 profiles between static and rolling approaches.

210 **3 Rolling Positive Matrix Factorization Setup**

211 **3.1 Data Validation & Xact PMF Matrix Preparation**

212 Over the year, airborne elements measured by the Xact contributed approximately 8% to the reconstructed PM_i mass at MRS-
213 LCP (S4: PM₁ Mass Reconstruction at MRS-LCP, Figs. S3 & S4). A total of 18 elements were selected for PMF analysis at
214 both sites (Figs. S1 & S2): S, Cl, K, Ca, Ti, V, Cr, Mn, Fe, Ni, Cu, Zn, As, Se, Br, Cd, Pb, along with Pd (specific to MRS-
215 LCP) and Rb (specific to FOS). Element selection was based on the proportion of data below MDLs (BDL), using a threshold
216 of 88 %, which is close to the 90 % BDL level applied in a previous Xact-PMF study at MRS-LCP (Camman et al., 2024).
217 This threshold is higher than the 70 % BDL criterion adopted in another Xact-PMF study (Manousakas et al., 2022), in order
218 to retain short but intense industrial events driven by anthropogenic markers such as Pb (82 % BDL at MRS-LCP). Some
219 exceptions were made to maintain a consistent set of elements across both sites. Specifically, Mn (90.8% BDL), Cd (92.7%
220 BDL), and Cr (94.6% BDL) at MRS-LCP were kept to match the elements used at FOS for homogeneous PMF analysis.
221 Another exception was made for Rb at FOS (96.3% BDL), which proved to be a relevant tracer for biomass burning emissions
222 during winter (Massimi et al., 2020). However, for the majority of elements, the BDL fraction was below 60% (Tables S2 &
223 S3).

224 The input matrix for the PMF analysis was constructed following the methodology proposed by Polissar et al. (1998b): values
225 below the MDL were replaced with MDL/2, and their associated uncertainties were set to 5/6 of the MDL. For values above
226 the MDL, the error was computed as the square root of the quadratic sum of the MDL and the estimated measurement
227 uncertainty from the Xact instrument (Reff et al., 2007; Camman et al., 2024). In addition, a cell-wise downweighting approach
228 was applied to data with a signal-to-noise ratio (SNR) below 2, as proposed by Visser et al. (2015b). For these low-SNR values,
229 the associated uncertainty was replaced with a penalized error defined by the function $2/\text{SNR}_{ij}$. The use of a cell-wise
230 downweighting of the error matrix, rather than classical variable-wise downweighting, allows for a more balanced integration
231 of the variables in the model, while primarily considering data points above the detection limit.

232 Short-lived events (1 h to 2-3 days), such as Sirocco episodes, construction activities, or fireworks, were excluded from the
233 dataset. These episodes disrupted factor analysis (e.g., Dust, Steel Industry) but could not be attributed to a specific factor due
234 to their chemical similarity with other sources (e.g., Saharan dust and local dust, fireworks and biomass burning). The
235 methodology for their identification and exclusion is described in S5: Data correction (Fig. S5).

236 The ToF-ACSM data at MRS-LCP were also analyzed for the same period using rolling PMF following the ACSM Standard
237 Operating Procedure established within the COLOSSAL project (COLOSSAL, 2021), as detailed in Chen et al. (2022) and
238 Chazeau et al., (2022). A total of five organic aerosol factors were resolved for the year 2023 (Fig. S6). Among them, the
239 Biomass Burning Organic Aerosol (BBOA), displayed marked seasonal variability, with no contribution observed between

240 May and September. The Hydrocarbon-like Organic Aerosol (HOA) factor was predominantly associated with traffic
241 emissions, while the Cooking Organic Aerosol (COA) factor originated from food preparation activities. Two additional
242 factors were attributed to long-range transported secondary organic aerosols: More Oxidized Oxygenated Organic Aerosol
243 (MOOOA) and Less Oxidized Oxygenated Organic Aerosol (LOOOA). These results are consistent with previous studies at
244 the MRS-LCP site (Chazeau et al., 2022) and will be used to support interpretations of elemental concentration variations.

245

246 **3.2 Static PMF analysis for Airborne Elements**

247 As limited information was available on Xact PMF factors in the region (Camman et al., 2024), static PMF analyses were first
248 performed to define reasonable PMF solutions. Each site was treated independently to ensure site-specific interpretation. PMF
249 solutions for the full 2023 dataset (YEAR), ranging from 5 to 12 factors, were evaluated to identify the most meaningful
250 configuration for each site. Statistical diagnostics (Q/Q_{exp} and unexplained variation, UEV) suggested optimal solutions of 9
251 factors for MRS-LCP and 8 for FOS (Fig. S7). However, examination of factor time series, daily trends, chemical composition,
252 and geographical origins indicated that the most environmentally interpretable solutions were obtained with 8 factors at MRS-
253 LCP and 9 at FOS (Table S4).

254 To investigate seasonal variability in source contributions, each PMF dataset was divided into 4 seasons: JF_D: January,
255 February, December, MAM: March, April, May, JJA: June, July, August, and SON: September, October, November.
256 Unconstrained preliminary runs revealed that some factors, such as the Cl-rich (4.2.7) and the Shipping (4.2.1), exhibited
257 strong seasonality at both sites and could not be clearly identified in some periods unless constrained. For instance, the Shipping
258 factor was not retrieved during winter at both sites (Tables S5 & S6), probably due to reduced sea breeze advection of shipping
259 plumes (Chazeau et al., 2021). Similarly, during JJA the Cl-rich factor was partly mixed with Dust in unconstrained runs
260 (Tables S5 & S6). Although Dust may contain some residual Cl (Visser et al., 2015b), this is not consistent with the other
261 seasons PMF results. On the other hand, the Shipping factor constrained during the winter season exhibits the same diurnal
262 pattern, characteristic of passenger ship activity (Fig. S21, 4.2.1), as observed in summer, confirming the year-round
263 environmental consistency of this factor.

264 To address these seasonal inconsistencies, following an approach similar to Chazeau et al. (2022), reference factor profiles
265 were extracted from PMF solutions with a higher number of factors. An 11-factor solution enabled the identification of the
266 Shipping factor during JF_D and a distinct Cl-rich factor during JJA. These reference profiles were subsequently used to
267 constrain the Shipping and Cl-rich factors during JF_D and JJA, respectively, using the α -value approach, with random α -
268 values ranging from 0 to 0.5 in steps of 0.05 for the static PMF analysis and bootstrap runs.

269 Unlike the OA rolling PMF, where BBOA is resolved only from September to May, the Xact rolling PMF retained a Biomass
270 Burning factor throughout the year. This choice reflects the expectation of year-round biomass burning emissions (e.g.,
271 wildfires, crop burning, barbecue) and avoids unrealistic redistribution of K into other factors. The relevance of this approach
272 is supported by the year-round presence of BC_{SF} and its consistent albeit low correlation with the final Biomass Burning factor

273 during summer ($R^2 = 0.21$ at MRS-LCP and $R^2 = 0.10$ at FOS), as well as still elevated Biomass Burning contribution (Fig.
274 S22).

275 To assess the statistical uncertainty of the factor profiles, each seasonal PMF solution was then bootstrapped 100 times. To
276 retain only environmentally meaningful runs, a set of custom criteria was applied to the bootstrap outputs. These criteria, based
277 on the tracer element apportioned to each factor, proved more effective in filtering out "mixed" or inconsistent solutions. The
278 complete list of criteria and associated thresholds for each PMF solution, as well as the percentage of retained bootstrap runs,
279 are provided in Supplements (Tables S7 & S8, respectively).

280

281 **3.3 Rolling PMF Parametrization**

282 To capture fine temporal variability of sources, rolling PMF was applied at both sites using the same dataset as for the static
283 PMF. As preliminary static PMF solutions showed high similarity for common factors at both sites (3.2), rolling PMF
284 parameter optimization was performed only for the MRS-LCP dataset. The resulting optimal settings were then applied to the
285 FOS dataset.

286 Canonaco et al. (2021) proposed a method to determine the best rolling PMF parameters. Rolling PMF implemented in SoFi
287 allows for adjustment of several key parameters, including rolling window size, number of PMF repeats per window, and the
288 number of days by which the window is shifted, in addition to static PMF options such as factor constraints and a-value
289 configuration. Similar to the approach used in Canonaco et al. (2021), we developed a method based on statistical indicators,
290 namely Q/Q_{exp} , percentage of unselected PMF runs and total UEV, to select optimal rolling PMF settings (rolling window size,
291 maximum a-value, and PMF repeats per window). Previous Rolling PMF study with ACSM datasets (Canonaco et al., 2021;
292 Chen et al., 2021) used the percentage of non-modeled data points to determine the minimum number of PMF repeats per
293 window required to ensure 0% non-modeled points. However, this criterion was not applicable here, as nearly all modeled
294 points met the selection criteria, even with a low number of repeats, likely due to differences in the selection criteria applied
295 in both studies. We used instead the percentage of unselected runs. Window sizes of 7, 14, 21, and 28 days were tested, with
296 the rolling window shifted by 1 day over the entire dataset. Maximal a-values of 0.2, 0.4, and 0.6 were explored, and PMF
297 repeats per window were set to 1, 5, 10, and 50 successively. As testing all combinations of the three parameters ($4 \times 3 \times 4 =$
298 48 rolling PMF tests) would require many days of computation on a modern multicore PC, each rolling PMF run taking
299 approximately 6 hours, we adopted a base-case configuration (rolling window size = 14 days, a-value = 0.4, PMF repeats per
300 window = 10). In each Rolling PMF test run, only one parameter was modified while the other two were held constant (base-
301 case values), following the approach of Canonaco et al. (2021).

302 The window size is a critical parameter in rolling PMF, as it determines the ability to resolve short-term temporal variability
303 of evolving factor profiles and to assess the lifetime of aerosol sources. Previous studies on organic aerosol PMF have
304 commonly selected 14-days windows (Parworth et al., 2015; Canonaco et al., 2021; Chazeau et al., 2022; Chen et al., 2022;
305 Via et al., 2022). In this study, statistical analysis (mean Q/Q_{exp} , percentage of unselected runs, and total UEV) indicated that

306 both 14-days and 21-days windows were acceptable (Fig. S8). However, some geochemical considerations supported the use
307 of a 21-days window. First, Xact provides direct elemental quantification; consequently, redox changes without a phase change
308 (e.g., $\text{SO}_2(\text{g})/\text{SO}_4^{2-}(\text{p})$) are not observable, whereas the ACSM captures organic aerosol oxidation through changes in m/z
309 signatures. As a result, metallic aerosol signals measured by Xact are expected to exhibit longer apparent atmospheric residence
310 times than organic aerosol components measured by the ACSM. Furthermore, the particularly dry conditions in 2023 (Météo-
311 France, 2023) limited wet deposition, and metals, primarily found in fine particles, typically exhibit longer atmospheric
312 lifetimes (Roy et al., 2019). Together, these factors justified selecting a 21-day window for the final analyses.

313 As shown earlier (3.2), the Cl-rich and Shipping factors showed strong seasonality and therefore required constraints. Unlike
314 the seasonal static approach, rolling PMF operates on the full annual dataset; reference profiles were thus selected from the
315 periods in which each factor was most robustly resolved (e.g. summer for Shipping and winter for Cl-rich, Tables S5 & S6).
316 Constraints were applied using randomly selected a-values, varying from 0 up to a maximum a-value in increments of 0.05.
317 The maximum a-value was tested at 0.2, 0.4, and 0.6. This narrower range, compared with that explored by Canonaco et al.
318 (2021), was chosen to avoid over-constraining the factors and to prevent unnecessary computational load. Sensitivity tests
319 showed that maximal a-value had minimal influence on the key statistical indicators (Fig. S8), and a maximum a-value of 0.4
320 was ultimately selected, consistent with the recommendations of Canonaco et al. (2021).

321 To determine the minimal number of PMF repeats per window, we evaluated both the percentage of unselected runs and the
322 minimum number of PMF repeats per modeled day while varying the total repeats per window, with bootstrapping enabled.
323 The percentage of unselected runs showed no significant variation with the number of PMF repeats per rolling window (Fig.
324 S8). While this metric provides a general indication of the statistical robustness of the rolling PMF parametrization, it does not
325 reflect the temporal variability in the model's ability to resolve source apportionment at specific times of the year. To better
326 assess this aspect, we evaluated the number of PMF repeats per modeled day in the final solution (Table S9). A minimum
327 threshold of 10 PMF repeats per modeled day was adopted, leading to a requirement of at least 50 PMF repeats per window.
328 Finally, the detailed study of several Rolling PMF solutions at MRS-LCP showed best environmental accuracy and statistical
329 stability for 21 days rolling window length, 1-day delay and 50 repetitions per window with maximal a-value set to 0.4.

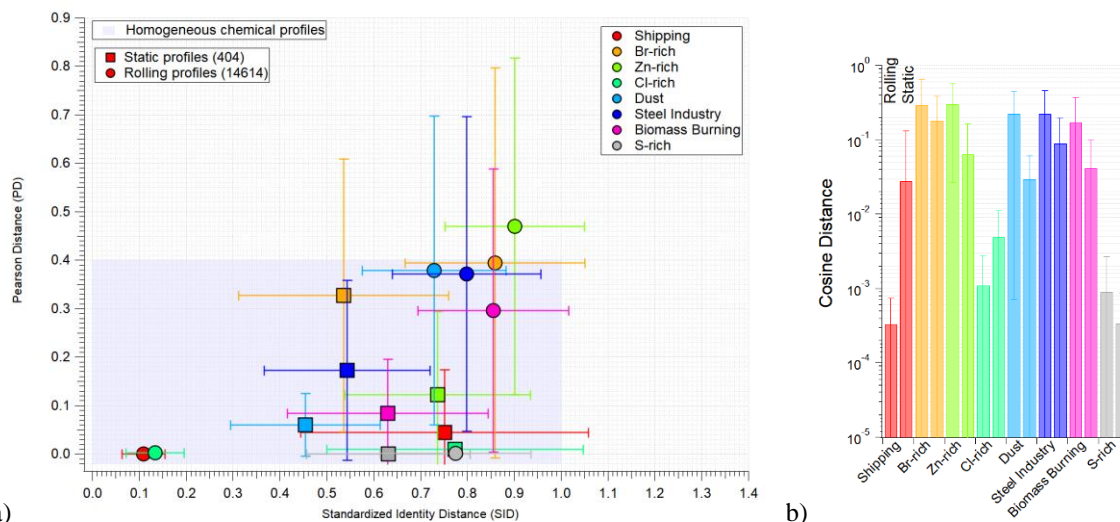
330 PMF factors at both sites were extracted using the same selection criteria as in the static analysis (3.2, Table S7), with additional
331 conditions to improve factor classification. Specifically, the selected factor's score had to exceed that of the second-highest
332 factor to avoid potential factor mixing, and each criterion score had to account for at least 30% of its specific tracer (≥ 0.3).
333 This additional condition was necessary to ensure a consistent classification of factors, especially given the wider variability
334 in criterion scores allowed by the rolling approach (Figs. S9 & S10). Notably, while this variability reflects the challenges of
335 applying selection criteria across the full annual dataset, it also highlights the strength of the rolling PMF method in capturing
336 the temporal variability in factor composition.

337

339 **4.1 Comparative analysis: static vs rolling PMF approach**

340 To compare factor profiles obtained from static and rolling PMF approaches, an extended analysis was performed for the eight
341 factors resolved at MRS-LCP using both methods (static PMF for YEAR, JF_D, MAM, JJA, and SON, and rolling PMF).
342 First, comparing elements apportionment for each method, shows that the rolling PMF leads to lower UEV for most elements
343 (Fig. S11). Furthermore, most factors, except the S-rich factor, exhibit higher S enrichment in the rolling solution, concomitant
344 with a reduced S contribution in the S-rich factor itself (Fig. S12). Such differences are particularly relevant given the wide
345 range of potential sources contributing to secondary sulfate formation (e.g., various industrial activities, shipping), while the
346 accurate attribution of the sulfate origins remains challenging (Chazeau et al., 2021; Su et al., 2025). The more homogeneous
347 S apportionment leads to enhanced sulfur enrichment in the Shipping and Br-rich factors at both sites, as well as in the Pb-
348 Industrial factor at FOS only, resulting in higher mass contributions of these factors in the rolling PMF solution across all
349 seasons (Fig. S13). An exception is observed for the Shipping factor at FOS during winter, where a higher contribution is
350 obtained with the static approach. However, the rolling PMF contribution appears more environmentally interpretable, given
351 the reduced sea-breeze advection during this period.

352 To further assess intra-variability of factor profiles resolved by static and rolling PMF, all factor profiles obtained at MRS-
353 LCP were extracted from the bootstrapped PMF outputs. This included 404 profiles from the static PMF analysis and 14,614
354 profiles from the rolling PMF analysis. Pairwise PD-SID and CD (2.3) were then calculated for each factor and each method
355 (8 factors \times 2 methods). For each factor, this resulted in $n(n-1)/2$ profile comparisons, where n is the number of profiles
356 obtained with a given PMF approach. Both PD-SID (Fig. 2a) and CD analyses (Fig. 2b) indicate larger variability in factor
357 profiles resolved by the dynamic approach compared to the static one, for both major (PD) and trace elements (SID). This
358 trend was observed for all factors except the constrained ones (Shipping, Cl-rich), highlighting the critical importance of
359 reference profile selection when applying constraints (3.2, 3.3). The S-rich factor showed relatively low PD enhancement and
360 CD under the rolling approach, consistent with the dominance of sulfur in the elemental mass and the persistence of large-
361 scale sulfate formation from photooxidation in the basin (4.2.9). By contrast, the Zn-rich factor exhibited PD-SID values above
362 the range of homogeneous chemical profiles, suggesting possible contributions from multiple sources, similar to what have
363 been stated in 4.2.6.



364

a)

b)

365 **Figure 2: a) PD-SID similarity plot of the factors obtained with the static (square) versus dynamic (round) PMF approaches. The**
 366 **blue shaded area shows the limit of the homogeneous chemical profile. For each point, round and square markers indicate the**
 367 **average distance from the $n(n-1)/2$ profile comparisons, and the error bars represent the standard deviation when comparing all**
 368 **pairs of factors for the 404 static profiles vs. the 14614 dynamic profiles. b) Cosine Distance similarity plot of the factors from both**
 369 **PMF approaches (rolling on the left, static on the right for each bar).**

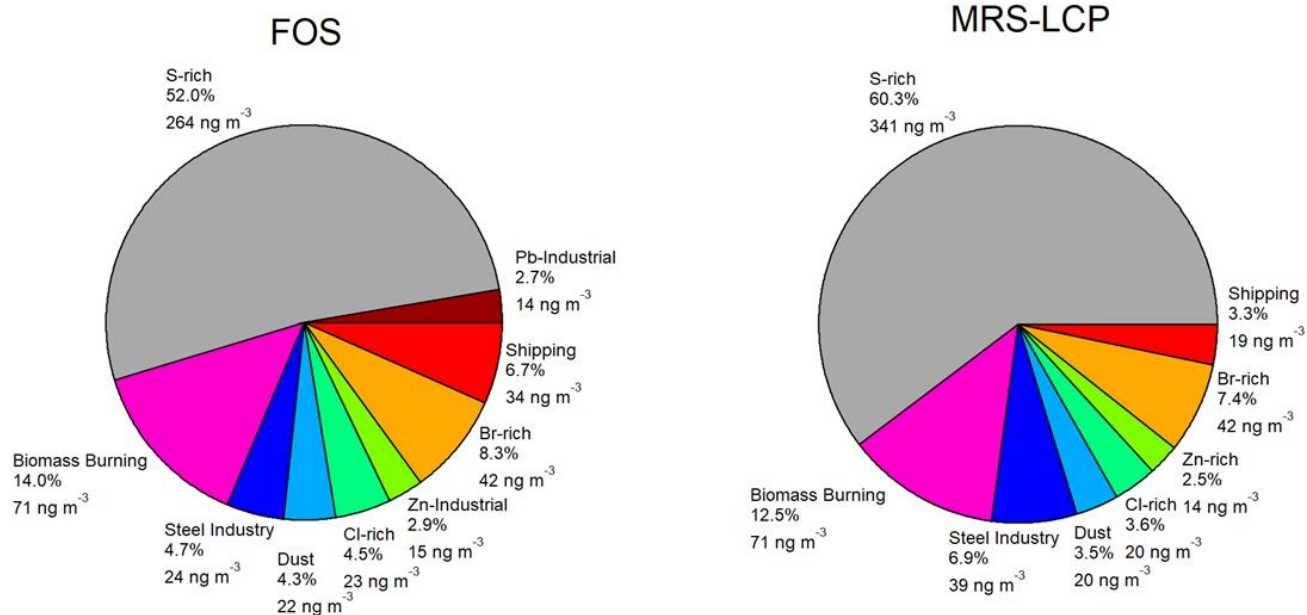
370 To assess the temporal variability of factor composition within the rolling PMF approach, PMF runs were attributed to
 371 individual days of the dataset. Using a 21-days window, a 1-day shift, and 50 PMF repeats per window, each day was
 372 represented by approximately 50 selected PMF runs (after applying the selection criteria; 3.3), corresponding to all rolling
 373 windows including that day. For each factor, daily rolling PMF profiles were compared to the corresponding static (YEAR)
 374 profiles by calculating the CD (Fig. S14). The mean and standard deviation of these metrics were then derived for each factor.
 375 In organic aerosol PMF studies, CD values above ~ 0.15 ($\theta > 30^\circ$) are generally considered indicative of weak similarity
 376 (Bougiatioti et al., 2014). The daily CD between rolling and static factor profiles shows minimal variation for the S-rich factor
 377 and for the constrained Shipping and Cl-rich factors, consistent with previous results. In contrast, the Br-rich, Zn-rich, Dust,
 378 Steel Industry, and Biomass Burning factors exhibit pronounced increases in CD (> 0.15) during specific periods of the year,
 379 indicating substantial temporal variability in source chemical composition that is effectively captured by the rolling PMF
 380 approach.

381 Detailed analyses of the daily CD for the Biomass Burning factor (Fig. S15) reveal large deviations during summer, associated
 382 with enhanced sulfur enrichment. This behavior is consistent with previously reported increases in S/K ratios with the aging
 383 of biomass burning emissions (Viana et al., 2013). These results support the interpretation that Biomass Burning is mainly
 384 driven by fresh and local residential heating during winter, whereas summertime rolling profiles reflect distant sources (e.g.,
 385 wildfires, agricultural burning, barbecuing), combined with enhanced photochemical conversion of SO₂ to particulate sulfate
 386 under higher solar radiation. In contrast, the static PMF approach yields a Biomass Burning factor largely dominated by

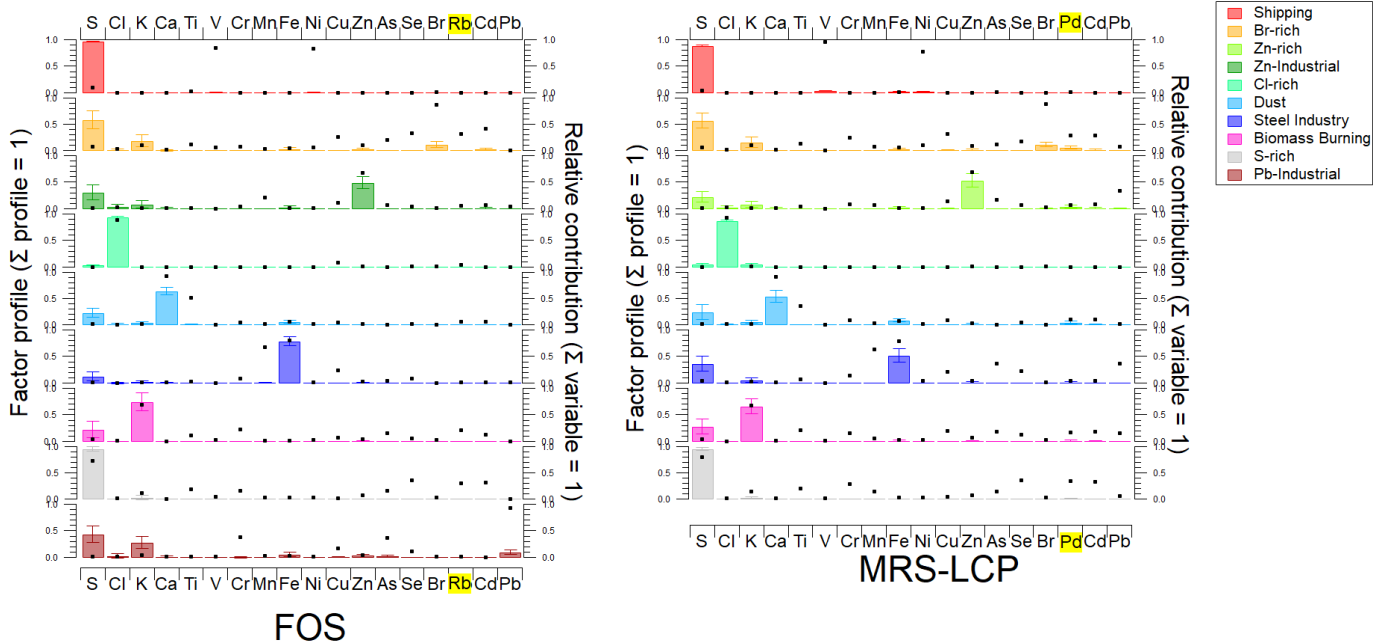
387 wintertime residential solid-fuel combustion and is therefore unable to adequately represent summertime biomass burning
388 emissions.

389 Overall, these results demonstrate the improved ability of the rolling PMF approach to capture seasonal variability and short-
390 term changes in aerosol composition. However, further work is needed to fully understand submicron airborne elements
391 sources in the region and to assess the geochemical relevance of short-lived rolling PMF profiles.

392 4.2 Interpretation of PMF factors

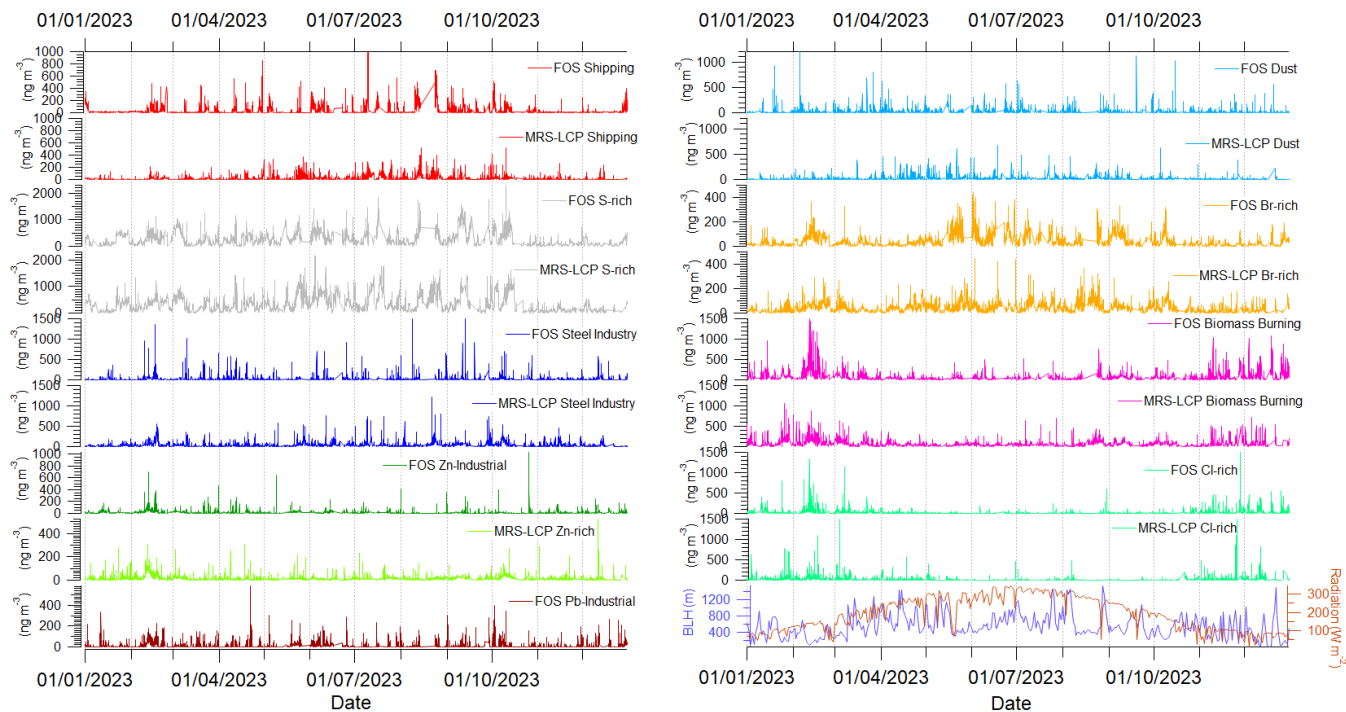


393
394 **Figure 3: Pie chart showing the average mass contribution of Xact rolling PMF factors for FOS (left) and MRS-LCP (right).**



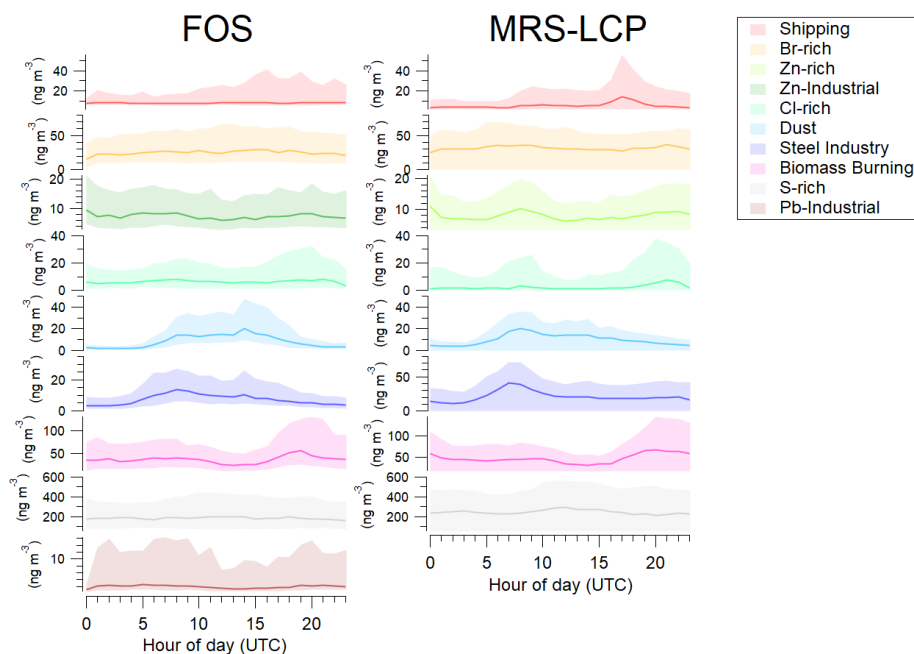
395
396
397
398

Figure 4: Final rolling PMF factors profile for FOS (left) and MRS-LCP (right). The colored bar plots represent factor profile contribution (left axis), while black markers indicate the relative contribution of each variable (right axis). The yellow-highlighted letters denote the two differing elements between both sites.



399

400 **Figure 5: Factors times series for the final rolling PMF solution. Shortwave radiation and boundary layer height (BLH) for the**
401 **Marseille-Fos basin area during the year 2023 were obtained from OpenMeteo (<https://open-meteo.com/>).**



402
403 **Figure 6: Diurnal patterns for FOS (left) and MRS-LCP (right). The colored lines represent the median diurnal evolution of each**
404 **factor, the dashed lines indicate the mean diurnal evolution, and the light-colored areas show the interquartile range.**

405 Rolling PMF analysis of PM₁ Xact data resolved nine factors at FOS and eight at MRS-LCP, including seven factors common
406 to both sites (Figs. 3-6, S16-S19). These shared factors comprised S-rich, Br-rich, and Cl-rich factors associated with secondary
407 aerosol formation, as well as Biomass Burning, Dust, Shipping, and Steel Industry. A Zn-rich factor was retrieved exclusively
408 at MRS-LCP, while two additional industrial factors (i.e. Zn-Industrial and Pb-Industrial) were identified only at FOS. No
409 distinct factor could be exclusively attributed to road transport emissions, as non-exhaust traffic-related metals are
410 predominantly associated with coarse particles (Bukowiecki et al., 2009; Visser et al., 2015; Pant et al., 2017). Nevertheless,
411 road transport may contribute to the Steel Industry and Zn-rich factors at MRS-LCP.

412 Secondary aerosols dominate the submicron elemental mass at both sites, with the S-rich factor accounting for more than half
413 of the total PM₁ elemental mass. Biomass Burning represents the second largest contribution. The Dust factor contributes less
414 than 5% at both sites, consistent with the predominance of crustal material in the coarse fraction (Pey et al., 2013a). Eventually,
415 direct anthropogenic sources, including industrial factors (Steel Industry, Pb-Industrial, Zn-Industrial) and Shipping, each
416 contribute less than 7% to the submicron elemental mass. Although these contributions to PM₁ mass are relatively small, their
417 potential health impact may be significant. Specifically, shipping and industrial combustion processes are known to emit
418 particles in the ultrafine size range (Jonsson et al., 2011; Riffault et al., 2015; Momenimovahed et al., 2021), which can
419 penetrate deeply into the respiratory system and cause adverse health effects (Kreyling et al., 2006).

420

421 **4.2.1 Shipping**

422 At MRS-LCP, shipping emissions contributed approximately 6% to total PM₁ during summer 2018 (Camman et al., 2024). In
423 this study, Shipping emissions contributed to 6.7% and 3.3% of the total element mass of the PM₁ at FOS and MRS-LCP,
424 respectively (Fig. 3). At both sites, this factor was composed mainly of sulfur ($\geq 89\%$) and accounted for the majority of V and
425 Ni ($> 88\%$, Fig. 4), consistent with previous ED-XRF shipping emissions studies in Marseille (Le Berre et al., 2025) and other
426 coastal cities (Scerri et al., 2018; Fossum et al., 2024). Slight Fe enrichment at MRS-LCP (2%) may reflect ship manoeuvring
427 at berth (Le Berre et al., 2025).

428 Non-Parametric Wind Regression (NWR, Figs. S16 & S17) analyses further confirmed the maritime origin of the Shipping
429 factor. At both sites, shipping plumes were advected inland by daytime sea breeze, especially between May and October (Figs.
430 6 & S20). Compared with MRS-LCP, the FOS site is less frequently influenced by sea-breeze circulation (Fig. S20), likely
431 intercepting shipping plumes more episodically and at a more aged stage. This is consistent with the higher sulfur fraction
432 observed at FOS ($96.8 \pm 0.6\%$) relative to MRS-LCP ($89.4 \pm 1.0\%$), reflecting enhanced secondary sulfate formation during
433 transport. The higher sulfur content also explains the larger average contribution of the Shipping factor at FOS (34 ng m^{-3})
434 compared with MRS-LCP (19 ng m^{-3} ; Fig. 3). Moreover, the industrial Fos-sur-Mer harbour hosts many tankers and cargo
435 vessels awaiting port entry, as well as by tankers transiting through the Berre Channel (MarineTraffic,
436 <https://www.marinetraffic.com>). The longer residence time of these vessels in the Gulf of Fos-sur-Mer may further contribute
437 to the observed sulfur enrichment. Daily cycles further reflected port-specific activities (Figs. 6 & S21). Marseille's port mainly
438 serves passenger ships, with peak ship movements in the early morning (4:00-7:00 UTC) and late afternoon (16:00-18:00
439 UTC), corresponding to two distinct peaks in the MRS-LCP shipping factor. In contrast, Fos-sur-Mer GPMM activity is
440 dominated by cargo traffic, and FOS Shipping factor exhibited a flatter diurnal profile, with a slight midday increase likely
441 driven by sea breeze rise rather than increasing shipping traffic.

442 Consistent with recent IMO regulations and desulfurized fuel increased use (Yu et al., 2021; Fossum et al., 2024), V/Ni ratios
443 have decreased compared to pre-IMO values (1.2 ± 0.2 at MRS-LCP, 1.6 ± 0.3 at FOS vs. approximately 2 in summer 2018;
444 Camman et al., 2024). The slightly higher ratio observed at FOS may reflect a stronger industrial influence or the continued
445 use of heavy fuel oil in combination with scrubbers on tankers and cargo vessels (Brezins et al., 2026a). Another consequence
446 of IMO 2020 regulation is that SO₂, once a reliable tracer of shipping emissions at MRS-LCP (Lu et al., 2006; Chazeau et al.,
447 2022), no longer correlated with the shipping factor in 2023, indicating effective reduction of SO₂ emissions.

448

449 **4.2.2 Biomass Burning**

450 The Biomass Burning factor was identified at both sites and contributed to more than 20% of the PM₁ elemental mass
451 concentration during winter (Fig. S22). It was primarily composed of K (> 66%) and S (> 22%), with trace elements such as
452 Rb (only at FOS, not calibrated in MRS-LCP), Cu, Cr, and As (Fig. 4).

453 Both sites exhibited typical daily cycles, with peak concentrations between 05:00-09:00 UTC and 19:00-23:00 UTC (Fig. 6),
454 reflecting increased night-time domestic heating. This trend closely aligns with the BBOA factor behavior reported at MRS-
455 LCP and in previous studies (Viana et al., 2013; Chazeau et al., 2022). NWR analyses showed a clear land-breeze influence
456 during winter, from the 5°-90° sector at both sites, consistent with biomass burning emissions transported by nocturnal land
457 breeze (Figs. S23-S24). At FOS, an additional contribution was observed from the southeast (125°-145°), possibly linked to
458 mixing with industrial combustion sources in the Port-de-Bouc area. During summer (JJA), the factor's geographical origin at
459 MRS-LCP suggests a stronger influence of local sources, whereas at FOS it exhibits a distinct southeast origin associated with
460 Pb-industrial activity (4.2.3), which may indicate partial redistribution of K from other sources during this period (Figs. S23-
461 S24).

462 Significant correlations with other combustion-related markers confirmed the origin of the factor. At MRS-LCP, it was
463 correlated with BC_{SF} (R = 0.78) and BBOA (R = 0.77), and particle number concentrations in the 150-200 nm range (R² =
464 0.59, Figs. S25-S26), consistent with the size of biomass burning aerosols, which typically range from approximately 100 nm
465 (fresh) to 250 nm (aged) (Janhäll et al., 2010). At FOS, good correlations were observed with BC_{SF} (R = 0.80) and benzene (R
466 = 0.69) (Fig. S27). However, benzene is also emitted by industrial sources: NWR analyses indicate that, while winter benzene
467 shows a minor northeastern contribution, summer patterns are dominated by emissions from the Fos-sur-Mer and Port-de-
468 Bouc industrial areas (4.2.3, Fig. S28). This suggests that the Biomass Burning factor at FOS may include a partial industrial
469 combustion contribution.

470 Finally, factor at both sites exhibited traces of As, Cr, and Cu, which could result from the combustion of wood treated with
471 Chromium-Copper-Arsenate (CCA), (Solo-Gabriele et al., 2002; Wasson et al., 2005), a pesticide historically used for timber
472 preservation (Morais et al., 2021). Although CCA has been banned for commercial use in Europe since 2004, some industrial
473 applications remain permitted, and no specific guidance has been provided regarding the incineration of CCA-treated wood
474 (COMMISSION DIRECTIVE 2003/2/EC of 06/01/2003).

475

476 **4.2.3 Pb-Industrial**

477 This factor was exclusively identified at the FOS site. It represents 2.7% of the yearly average of the total elemental mass. It
478 was primarily composed of S (44%) and K (28%) and accounted for 93% of the total Pb mass (Fig. 4). It did not exhibit any
479 clear seasonal or diurnal variability (Figs. 6 & S22). Nevertheless, the NWR analysis revealed distinct contributions from the
480 235°-260° and 110°-150° sectors under relatively strong wind conditions, as well as a minor contribution from the 5°-90°

sector during winter only (Figs. S17 & S29). This latter contribution, typical of nocturnal land breeze transport, suggests a possible influence from residential solid fuel combustion (4.2.2). The presence of Cr, Cu, and As traces, similar to the Biomass Burning factor, further supports this potential mixing of biomass burning and industrial combustion. However, the predominant southwesterly and southeasterly origins are indicative of industrial sources, likely associated with the Fos-sur-Mer and Port-de-Bouc industrial complexes, respectively.

Fine airborne Pb has long been recognized as a marker of anthropogenic activities (Clements et al., 2014; Riffault et al., 2015), and may originate from coal combustion (Alastuey et al., 2016; Rai et al., 2021), industrial processes (Moffet et al., 2008; Manousakas et al., 2022), and waste incineration (Riffault et al., 2015). In the area, coal combustion is exclusively associated with the steel industry in Fos-sur-Mer and therefore cannot account for the southeastern Pb contribution. A municipal waste incinerator located near the steel complex in Fos-sur-Mer, together with petrochemical and plastic-processing facilities in the Port-de-Bouc industrial area, where open burning has been reported, likely account for the observed Pb, As, and Cd emissions (Valavanidis et al., 2008; Kumar et al., 2015).

Overall, the elemental composition, dominated by S, K, Pb, and As, and the observed wind directions suggest a combustion-related industrial source. Note that the Pb NWR at MRS-LCP indicates a dominant local and north-easterly origin, inconsistent with an industrial influence from the Berre Pond area (Fig. S30). Nevertheless, a partial contribution from the west, confirms an influence of industrial Pb at MRS-LCP. This signal was largely captured within the Steel Industry factor but was not sufficient to resolve a distinct Pb-Industrial factor at this site (Fig. 4).

498

499 **4.2.4 Steel Industry**

A factor enriched in Fe (FOS: 80%, MRS-LCP: 51%) and S (FOS: 12%, MRS-LCP: 37%) was identified at both sites accounting for the majority of Mn mass (>64%) (Fig. 4). This factor represents 4.7% and 6.9% of the total element mass of the PM₁ at FOS and MRS-LCP, respectively. At FOS, it clearly shows an origin from the 235°-260° sector aligning the steel industry in Fos-sur-Mer (Fig. S17). Furthermore, the presence of spikes in the time series (Fig. 5) strongly suggests an origin of intense and nearby industrial activity (Ledoux et al., 2006; Moreno et al., 2011a; Taiwo et al., 2014b; Almeida et al., 2015; Kfoury et al., 2015; Rai et al., 2020b; Rai et al., 2021). This is not surprising as the Berre Pond hosts one of the largest steel plants in France, located at approximately 2km from the FOS sampling site (Fig. 1).

A previous study (Sylvestre et al., 2017) characterized fine particulate emissions downwind of this facility associated with high levels of Fe, S, Mn, and Zn (Fig. S31), further supporting this source attribution. However, the Mn/Fe ratios observed here (FOS: 0.012; MRS-LCP: 0.006) are lower than those reported by Sylvestre et al. (2017) (0.056). This discrepancy likely reflects differences in particle size fraction (PM_{2.5} in Sylvestre et al. (2017) versus PM₁ in the present study), as well as potential mixing of this factor with other Mn- and Fe-containing sources at MRS-LCP.

Notably, neither railway nor road transport emissions could be attributed to a single PMF factor at MRS-LCP, whereas the St-Charles train station is only approximately 1km (260° direction) from MRS-LCP and the station is located in the city center

514 where massive road traffic occurs (Fig. 1). Nevertheless, the presence of a local contribution (Fig. S16), together with reduced
515 concentrations during weekends (Fig. S18), suggests a partial influence from road transport emissions (Manousakas et al.,
516 2022, 2025) in the Steel Industry factor at MRS-LCP. However, as previously observed at this site (Camman et al., 2024),
517 non-exhaust traffic emissions are only weakly captured in the submicron fraction, since tire and brake wear particles are
518 predominantly associated with particle sizes larger than 1 μm (Bukowiecki et al., 2009; Visser et al., 2015; Pant et al., 2017).
519 The northwestern and southwestern contributions of the factor at MRS-LCP (Fig. S16), associated with Mistral and sea breezes
520 advection, respectively, suggest a factor primarily related to steel industry emissions originating from the Fos-sur-Mer
521 industrial area. It was also marked by a sharp increase in diurnal activity between 04:00 and 07:00 UTC, followed by a gradual
522 decline, relative to the onset of sea breeze (Chazeau et al., 2021, Fig. 6). In both cases, oxidation of industrial plumes and
523 secondary sulfate formation from industrial SO_2 emissions can occur (Marris et al., 2012; El Haddad et al., 2013; Chazeau et
524 al., 2021), inducing S factor enrichment and higher average mass contribution of the factor at MRS-LCP (Fig. 3). The
525 additional presence of Pb in the MRS-LCP factor is consistent with previous findings at this site (Camman et al., 2024) and
526 may reflect the inability of PMF to separate Pb-related industrial emissions (4.2.3) from the Steel Industry emissions, due to
527 the spatial proximity of these emission sources.

528

529 **4.2.5 Zn-Industrial (FOS)**

530 A factor composed of $\text{Zn} > \text{S} > \text{K} > \text{Fe} > \text{Mn} > \text{Cu} > \text{As}$, in decreasing order of abundance was identified at FOS (Fig. 4),
531 representing 2.9% of the total elemental PM_{10} mass on a yearly average at this site. Airborne Zn has been previously attributed
532 to several sources, including road transport, often associated with Sb (Camman et al., 2024; Manousakas et al., 2025; Charron
533 et al., 2019), industrial processes (Manousakas et al., 2022; Riffault et al., 2015), waste incineration, particularly when
534 associated with Pb and Cl (Moffet et al., 2008; Enestam et al., 2011), and solid fuel combustion (Tissari et al., 2015; Rai et al.,
535 2020). NWR analysis indicated a dominant contribution from the 235° - 260° sector (Fig. S17), corresponding to the industrial
536 zone of Fos-sur-Mer, where both a major steel plant and the waste incinerator are located. A minor contribution from the 10° -
537 50° sector suggests influence from land breezes, possibly associated with sea-breeze return flow at night (Drobinksi et al.,
538 2007). According to the 2023 French Pollutant Release and Transfer Register (IREP,
539 <https://www.georisques.gouv.fr/donnees/bases-de-donnees/installations-industrielles-rejetant-des-polluants>), the steel plant in
540 Fos-sur-Mer is the largest regional source of Zn emissions. Factor enrichment with Mn further supports its attribution to the
541 steel industry (4.2.4). However, Zn emissions from steelmaking are typically associated with electric arc and basic oxygen
542 furnaces (European Commission, 2008), while the Fos-sur-Mer facility reportedly operates a blast furnace. Furthermore, no
543 correlation was observed between the Zn-Industrial factor and the Steel Industry factor, which may reflect emissions from
544 distinct processes within the same facility. Enrichment in K and S also indicates a potential contribution from waste
545 incineration. Overall, the diverse geographical origins and mixed chemical composition suggest that the Zn-Industrial factor

546 represents a mixing of multiple sources, including steel industry and waste incineration. Despite the clearly distinct sources,
547 PMF was unable to resolve multiple Zn-enriched factors.

548

549 **4.2.6 Zn-rich (MRS-LCP)**

550 A Zn-rich factor, dominated by Zn (53%) with notable contributions from S and K, was identified at MRS-LCP (Fig. 4),
551 accounting on average for 2.5% of the annual PM₁ elemental mass. Its daily cycle (Fig. 6), characterized by morning and
552 evening peaks, is similar to that of Biomass Burning factor (4.2.2) and to road transport rush hours. As discussed in 4.2.5,
553 various anthropogenic activities can contribute to airborne Zn emissions. However, its northeastern origin under low wind
554 conditions suggests a source advected by nocturnal land-breeze (Chazeau et al., 2021, Fig. S16), ruling out an industrial origin
555 from Fos-sur-Mer (4.2.5). A previous study at MRS-LCP associated a submicron Zn-enriched factor with tire and brake wear,
556 based on the presence of Sb (Camman et al., 2024). In the present study, Sb was excluded due to a high proportion of
557 measurements BDL (96%). Although Cu can serve as a tracer of non-exhaust traffic emissions (Dubois et al., 2025), the Zn-
558 rich factor shows little enrichment in Cu. This likely reflects the fact that metallic tracers of non-exhaust emissions are
559 predominantly associated with particles larger than 1 μm (Pant et al., 2017). Weak correlations with HOA and BC_{LF} (R < 0.35)
560 further exclude road traffic emission as a major contributor (Fig. S25). Instead, the presence of K, similar to the Biomass
561 Burning factor (4.2.2), together with its daily cycle (Fig. 6) and land-breeze transport, point to solid fuel combustion as a
562 possible source. Nevertheless, its moderate seasonal variability (Fig. S22), its daily cycle (Fig. 6) and substantial contribution
563 to Pb concentrations (34%) suggest little influence from waste incineration and indicate that this factor cannot be attributed to
564 a single dominant source. Rather, it likely reflects a mixture of Zn-containing emissions, including combustion-related sources
565 (e.g., biomass burning; Tissari et al., 2015), residual traffic emissions (Camman et al., 2024), and potentially waste-related
566 activities (Enestam et al., 2011). Analysis of the factor chemical composition at different periods of the year (e.g., February
567 and May) reveals marked seasonal variations in factor composition (Fig. S32), with higher enrichment in Fe and Ca in May,
568 and increased contributions of K, S, Cl, and Br in February. This variability suggests changing source influences, with a
569 stronger contribution from road dust and non-exhaust traffic emissions during warmer periods and enhanced contributions
570 from combustion-related and secondary processes in winter (4.2.2, 4.2.7, 4.2.8). The northeastern sector origin (5°-90°) further
571 supports the influence of locally transported and mixed aerosols, likely associated with nocturnal thermal breeze recirculation
572 processes (Drobinski et al., 2007).

573

574 **4.2.7 Cl-rich**

575 A Cl-rich factor, composed almost entirely of elemental Cl (FOS: 94%, MRS-LCP: 88%), was identified at both sites and
576 accounted for at least 87% of elemental Cl mass (Fig. 4), and 4.5% and 3.6% of the total elemental mass on a yearly average
577 at FOS and MRS-LCP, respectively. It exhibited a strong seasonal pattern, with low average concentration in summer (<10 ng

578 m⁻³ at both sites) and higher average concentration in winter (FOS: 46 ng m⁻³; MRS-LCP: 40 ng m⁻³, Fig. S22). Such seasonality
579 is consistent with previous studies linking fine particulate chloride to combustion-related emissions or secondary formation
580 from gaseous chlorine species (Visser et al., 2015b; Le Breton et al., 2018; Tobler et al., 2020; Rai et al., 2021; Chazeau et al.,
581 2021; Wang et al., 2023; Pawar et al., 2023; Masoud et al., 2023). Primary sources of particulate and gaseous chlorine include
582 biomass burning (e.g. KCl, NH₄Cl), coal combustion, crop residue burning, industrial activities (e.g. Cl-VOCs, steel industry),
583 and sea salt dechlorination (Keene et al., 1999; Wang et al., 2017; Ding et al., 2020; Peng et al., 2021). Chlorine gases may
584 further react with NO_x and N₂O₅, leading to ClNO₂ formation in particle phase, followed by rapid partitioning into the gas
585 phase (Thornton et al., 2010; Simpson et al., 2015; Le Breton et al., 2018; Ahern et al., 2018). Combustion processes often
586 emit chlorine alongside NO_x, promoting ClNO₂ production. Other reactive intermediates such as Cl₂ and NOCl may also
587 contribute to photochemically active Cl atom formation (Jordan et al., 2015).

588 The pronounced diurnal variability of the Cl-rich factor, peaking in the early morning and evening, with a sharp increase
589 overnight and minimal activity around midday, indicates rapid ClNO₂ partitioning into the gas phase (Simpson et al., 2015;
590 Faxon et al., 2015; Le Breton et al., 2018; Wang et al., 2022; Wang et al., 2023; Pawar et al., 2023). This daily cycle is also
591 similar to that of the Biomass Burning, BC_{SF}, and chlorinated compounds from the ACSM and AE33 measurements (Fig. 6 &
592 S33). Both seasonal and diurnal behaviours (Figs. 6, S22 & S33) support the attribution of the Cl-rich factor to secondary
593 formation processes from gaseous chlorine species, mainly driven by combustion activities. At FOS, the Cl-rich factor
594 correlated with both the Biomass Burning factor (R² = 0.41, Fig. S34) and Chlorinated Volatile Organic Compounds (Cl-
595 VOCs) associated with industrial activity (1,2-dichloroethyl: R = 0.57; tetrachloroethyl: R = 0.46, Fig. S27), pointing to a
596 mixed origin.

597 Cl-rich factor originating from various wind directions at both sites (Figs. S16 & S17) further supports a mixed origin of the
598 factor, with a minor northeast contribution suggesting influence from biomass burning transported via nocturnal land breeze.
599 A small contribution from the marine areas may indicate partial influence from sea salt dechlorination, although this was not
600 considered a major source of fine particulate chloride in this study (S6: Sea Salt Dechlorination, Figs. S35-S36).

601

602 **4.2.8 Br-rich**

603 A second halogen-enriched factor was identified at both sites, though with a different composition. The Br-rich factor is
604 primarily composed of S (>57%) and K (>17%), and is highly enriched in Br (88% of Br at both sites) (Fig. 4). It represents
605 8.3% and 7.4% of the PM₁ elemental mass on a yearly average at FOS and MRS-LCP, respectively. Its moderate seasonal,
606 diurnal, and weekly variabilities (Figs. 6, S18, S19 & S22), in contrast to the Cl-rich factor (4.2.7), reflects a persistent
607 background contribution, consistent with previous observations at MRS-LCP (Camman et al., 2024). However, similar to the
608 Cl-rich factor, NWR analysis (Figs. S16 & S17) revealed diverse origins for this factor. At both sites, enhanced contributions
609 from marine sectors (south at FOS and southwest at MRS-LCP) suggest a partial influence from marine bromine emissions.
610 In particular, previous work in Fos-sur-Mer area has shown that chlorinated seawater is widely used for industrial cooling and

611 ballast water treatment in cargo vessels, leading to elevated bromoform concentrations at the sea surface in the vicinity of
612 industrial and port activities (from 0.22 to 10.22 ng m⁻³; Quivet et al., 2022). A similar practice in passenger vessels may occur
613 at Marseille harbour. Reactive bromine species can then undergo atmospheric reactions to form particulate brominated
614 compounds (Kothai et al., 2011; Simpson et al., 2015). At FOS, the southwestern origin also corresponds to the port-industrial
615 area hosting a coal-powered blast furnace, suggesting a potential contribution from particulate Br formed via reactive bromine
616 gases emitted during coal combustion (Lee et al., 2018; Rai et al., 2021; Peng et al., 2021).

617 At MRS-LCP, the Br-rich factor showed a major contribution from the southeast sector (105°-135°) under elevated wind
618 speeds, corresponding to two synoptic regimes: Sirocco (removed from the dataset, 3.1, Fig. S5) and the “Marine” wind,
619 typically observed during fall and spring (Chazeau et al., 2021). Although observed only occasionally, the “Marine” wind
620 travelled extensively over the Mediterranean Sea, potentially contributing to the sulfur and bromine enrichment of this factor.
621 Another potential contributor is a chemical facility located approximately 10 km east of MRS-LCP, along the 105° sector (Fig.
622 1), which has reported bromine use and past incidents involving gaseous bromine leaks (bouches-du-rhône.data.gouv.fr, 2013;
623 <https://www.georisques.gouv.fr>). Finally, minor contributions from the northeast sector (5°-90°) suggest aerosol nocturnal
624 transport with sea-breeze return flow, similar to the Zn-rich and the Cl-rich factors (4.2.6 and 4.2.7) (Drobinski et al., 2007),
625 further supporting the secondary origin of this factor.

626

627 **4.2.9 S-rich**

628 The S-rich factor is by far the most abundant (Fig. 3), contributing to more than 50% of the total measured elemental mass on
629 a yearly average for both sites. It is mainly composed with S (95%), elevated Se traces (approximately 35% of Se) at both
630 sites, and accounts for 73% and 79% of elemental S mass at FOS and MRS-LCP, respectively (Fig. 4). The S-rich aerosols are
631 typically attributed to oxidation of SO₂ to sulfate (SO₄²⁻) or to direct sulfate emission (Visser et al., 2015b; Rai et al., 2020a,
632 2020b; Rai et al., 2021; Manousakas et al., 2022, 2025), originating from both local industrial and port activities as well as
633 regional shipping emissions across the Mediterranean basin (Chazeau et al., 2021).

634 Notably, S-enriched factors are often associated with Se (Weber et al., 2019), as both elements share major anthropogenic
635 sources, such as metals production, coal, fuel, and biomass combustion, as well as natural sources such as sea salt and volcanic
636 activity (Eldred, 1997; Kuittinen et al., 2024; Su et al., 2025). Both elements are primarily emitted into gas phase then converted
637 to particulate forms at different rates, leading to decreasing Se/S ratios with aerosol ageing (Zhuang et al., 1999; Wen &
638 Carignan, 2007; Liu et al., 2021). In this study, Se/S ratios were 1.9×10^{-4} at FOS and 1.2×10^{-4} at MRS-LCP, within the
639 lower range of previously reported values (1.7×10^{-4} in PM_{2.5}, Kumar et al., 2025; 3.2×10^{-4} in PM₁₀, Rai et al., 2020b). In
640 the area, the only identified coal combustion source is the blast furnace of the steel industry in Fos-sur-Mer, but those ratios
641 suggest limited influence from coal combustion emissions.

642 NWR analysis points to a dominant contribution from the sea at both sites (Figs. S16 & S17), consistent with particulate S
643 emissions from shipping and sea water, or secondary formation in the port-areas of the Marseille-Fos basin. Previous work at

644 MRS-LCP reported elevated sulfate levels from major shipping routes, highlighting the continued importance of shipping
645 emissions in sulfate production (Chazeau et al., 2021), even after SO₂ reductions (4.2.1). The implementation of IMO
646 regulations has led to a substantial decrease in SO₂ emissions from shipping (up to ~77%; IMO), limiting its use as a direct
647 tracer of shipping activity compared to earlier studies at this site (Chazeau et al., 2022). However, the potential use of scrubbers
648 may still result in direct sulfate emissions from ships (Kuittinen et al., 2024), thereby partially maintaining the shipping
649 contribution to sulfate. Overall, while shipping-related SO₂ emissions have likely decreased, industrial activity and regional
650 transport of aged marine emissions over the Mediterranean remain important contributors to sulfate observed at MRS-LCP.
651 Assuming all S is in the form of SO₄²⁻, reconstructed sulfate from elemental S (Xact) strongly correlates with non-refractory
652 SO₄²⁻ from ToF-ACSM (R² = 0.91, slope = 0.99; Fig. S37). This confirms that sulfates are the dominant particulate form of
653 sulfur measured by the Xact, in line with findings across Europe (Furger et al., 2017: R² = 0.85, slope = 1.32, Xact in PM₁₀
654 and ACSM in PM₁; Tremper et al., 2018: R² = 0.93, slope = 1.41, Xact in PM_{2.5} and ACSM in PM₁). The larger slopes observed
655 in previous studies likely reflect differences in particle size fractions sampled by the Xact and ACSM instruments, while
656 operating both instruments in PM₁ led to reduced size-related biases in this study. Time series at both sites and ToF-ACSM
657 SO₄²⁻ at MRS-LCP indicate an optimal sulfate production period from January to mid-October, followed by a sharp decline,
658 likely linked to a sudden meteorological shift after a Sirocco event in mid-October (Fig. S38). Seasonal and diurnal patterns
659 (enhanced activity between 10:00-15:00 UTC, coinciding with peak solar radiation; Figs. 6 & S38) confirm that this factor is
660 strongly driven by secondary sulfate formation under high photochemical activity and stagnant conditions (El Haddad et al.,
661 2013; Salameh et al., 2015; Chazeau et al., 2021).

662

663 **4.2.10 Dust**

664 The Dust factor is primarily composed of Ca (>50%), with significant contributions from Ti at both sites (FOS: 51%, MRS-
665 LCP: 35%), alongside contributions of S, Fe, and K (Fig. 4). Although crustal material is generally associated with coarse
666 particles (Pey et al., 2013), mechanical processes such as sandblasting may also explain its presence in the PM₁ fraction (Gomes
667 et al., 1990). However, this factor contributed only modestly to PM₁ elemental aerosol mass (<5%) at both sites (Fig. 3).

668 Dust can refer to various sources, including: a) Short-range resuspension dust, linked to road dust or construction activities
669 (Belis et al., 2011; Dall'Osto et al., 2013; Visser et al., 2015b; Manousakas et al., 2022), b) Medium-range transported dust
670 such as industrial dust (Riffault et al., 2015, Almeida et al., 2020) or construction dust, and c) Long-range transport of crustal
671 material with strong wind regimes like the Mistral or Sirocco (Flaouanas et al., 2009). NWR analyses at both sites point to a
672 dominant contribution from crustal material transported during Mistral episodes (275°-360° sector, Figs. S16 & S17).
673 However, the observed diurnal and weekly patterns display daytime peaks predominantly on weekdays, consistent with local
674 resuspension processes driven by road traffic (Figs. 6, S18 & S19). These cycles are also similar to those of the Steel Industry
675 factor at both sites (4.2.4), suggesting possible partial mixing between the two sources. This is also supported by the partial
676 235°-260° sector origin of the factor at FOS, and by the reported elevated Ca concentrations downwind of the blast furnace

677 unit at the Fos-sur-Mer steel industry facility (Sylvestre et al., 2017, Fig. S17 & S31). This is consistent with previous findings
678 indicating a mixture of dust and steel industry emissions, obtained with source apportionment approach (Taiwo et al., 2014b).

679 **5 Conclusion**

680 This year-long source apportionment study at two sites provides a comprehensive picture of submicron elemental aerosols
681 across the Marseille-Fos basin using high-resolution Xact PM₁ measurements combined with a dynamic rolling PMF approach.
682 The sites, MRS-LCP (urban background) and FOS (industrial), are located on opposite sides of the basin, and are influenced
683 by complex regional meteorological conditions that facilitate inter-site aerosol transport. A novel dynamic source
684 apportionment approach was applied using a 21-day rolling window PMF via the SoFi Pro toolkit. This dynamic framework
685 allowed a more realistic representation of changing emission patterns compared with a static PMF and atmospheric processes
686 in a complex coastal-industrial environment characterized by frequent wind shifts and inter-site air mass exchanges.

687 The analysis resolved nine PMF factors at FOS and eight at MRS-LCP, with seven factors common to both sites. Among these
688 seven factors, three were attributed to secondary aerosol formation: S-rich factor (FOS: 52%, MRS-LCP: 60.3%), Cl-rich
689 (FOS: 4.5%, MRS-LCP: 3.6%), and Br-rich (FOS: 8.3%, MRS-LCP: 7.4%). Biomass burning was the second-largest
690 contributor at both sites (FOS: 14%, MRS-LCP: 12.5%). As expected given the intense harbour activity in the region, a
691 shipping factor was identified (FOS: 6.7%, MRS-LCP: 3.3%), with episodic peaks exceeding 400 ng m⁻³ that can last 1-3
692 hours. A dust-related factor, linked to both long-range transport and local resuspension, was also observed at both sites (FOS:
693 4.3%, MRS-LCP: 3.5%). A non-ascribed Zn-rich factor was retrieved exclusively at MRS-LCP (2.5%), while two additional
694 industrial factors were resolved only at FOS: a Pb-Industrial factor (2.7%) and a Zn-Industrial factor (2.9%), associated with
695 waste incineration and steel production. A Steel Industry factor was also identified at MRS-LCP (6.9%), though with
696 differences in composition. These differences suggest both mixing of industrial emissions and the formation of secondary
697 aerosols during plume transport from FOS to MRS-LCP. These results clearly demonstrate that emissions from the Fos-sur-
698 Mer industrial area influence air quality throughout the basin, transported under alternating Mistral and sea-land breeze
699 regimes.

700 Ten distinct elemental sources were characterized in the MRS-FOS basin, five of which (Shipping, Biomass Burning, Pb-
701 Industrial, Zn-Industrial, and Steel Industry) stem directly from primary anthropogenic emissions. The predominance of
702 human-related sources underscores the strong industrial and maritime imprint on the region's atmospheric composition. This
703 issue is further amplified by the basin's topography and population density, which enhance population exposure to a complex
704 mixture of potentially harmful airborne elements. Considering recent epidemiological findings linking residence near the Berre
705 industrial zone with increased chronic disease prevalence, including cancer and diabetes (Jeanjean et al., 2022), the present
706 results call for closer integration between atmospheric chemistry and health research. Future studies should focus on the toxic
707 potential of these resolved submicron sources to better quantify their public health implications in industrialized coastal
708 regions.

709 **Financial support**

710 This study received funding from the French Agence Nationale de la Recherche (ANR) programme under grant agreement no.
711 ANR-21-CE22-0015 (SHIPAIR). This study was also supported by AtmoSud for funding analytical instruments.

712 **Data availability**

713 All the Rolling PMF Xact results from this work can be accessed through Zenodo:
714 https://zenodo.org/records/18374331?preview=1&token=eyJhbGciOiJIUzUxMiIsImhhdCI6MTc2OTQyMjU3NywiZXhwIjozNzk4Njc1MTk5fQ.eyJpZCI6IjMjA5Y2EyLWI4MTgtNGY5OS05OGE1LTZmODEzZmZzZmU4OSIsImRhdGEiOnt9LCJyYW5kb20iOiI4ZDZjNzdiM2IxYzQ1NTNjY2VlOWY2NTc1Y2F1OWFkMiJ9.NS24rtFIWO69UgWBLj1GMT8ZlPx1z7_zgOkPO8qTs6auczRuKN8xJ5_avWt48Sx5bbPZtED3S2faC0cuIvcRCA (preview link).

718 **Code availability**

719 The PD-SID and CD code used in this work can be accessed through Zenodo:
720 https://zenodo.org/records/18374331?preview=1&token=eyJhbGciOiJIUzUxMiIsImhhdCI6MTc2OTQzNDkyMSwiZXhwIjozNzk4Njc1MTk5fQ.eyJpZCI6IjdlN2ZlMzllLWY5NWUtNGU4NS04YTUyY2YzMDk0MCI6ImRhdGEiOnt9LCJyYW5kb20iOiI0ZDdjZWQ1MGVhYzA4NDkyYTM1YWJiY2VkNTliMDY2ZiJ9.Z_BiknPu-cS7-HVb6kMgWxmKRh4QYrjsRvbS4k8bw20gs1P28oPc5dzMm1ufNhsF4sHN3J_e9cWYqpBR6LcJvQ (preview link).

724 **Author contributions**

725 MB, BC, NM, JLJ, GU, and BDA conceived the study. AD, GG, and RB provided technical assistance during the experiments.
726 AP provided the Xact instrument used for measurements at the FOS site. RB supported the deployment of the Xact instrument
727 at the FOS measurement site. AD contributed to the Xact data analysis. BC conducted the ToF-ACSM data analysis. MB
728 conducted the Xact data analysis and wrote the paper, with contributions from all of the co-authors.

729 **Competing interests**

730 The contact author has declared that none of the authors has any competing interests.

731 **Acknowledgements**

732 The authors would like to thank AtmoSud technical team and Brice Temime-Roussel for instrument maintenance and
733 calibration at the FOS and MRS-LCP stations. Mathilde Brezins also would like to thank Anna Tobler and Francesco Canonaco

734 for their regular support and assistance with SoFi toolkit debugging. Mathilde Brezins acknowledges the use of the ChatGPT
735 AI tool for Python script correction and for proofreading and grammar improvement during the manuscript preparation. All
736 outputs were reviewed and edited by Mathilde Brezins, who takes full responsibility for the final content. All of the final
737 wording reflects Mathilde Brezins's own edits and judgement.

738 **References**

- 739 Ahern, A. T., Goldberger, L., Jahl, L., Thornton, J., and Sullivan, R. C.: Production of N₂O_x and ClNO₂ through Nocturnal
740 Processing of Biomass-Burning Aerosol, *Environ. Sci. Technol.*, 52, 550–559, <https://doi.org/10.1021/acs.est.7b04386>, 2018.
- 741 Alastuey, A., Querol, X., Aas, W., Lucarelli, F., Pérez, N., Moreno, T., Cavalli, F., Areskou, H., Balan, V., Catrambone, M.,
742 Ceburnis, D., Cerro, J. C., Conil, S., Gevorgyan, L., Hueglin, C., Imre, K., Jaffrezo, J.-L., Leeson, S. R., Mihalopoulos, N.,
743 Mitosinkova, M., O'Dowd, C. D., Pey, J., Putaud, J.-P., Riffault, V., Ripoll, A., Sciare, J., Sellegri, K., Spindler, G., and Yttri,
744 K. E.: Geochemistry of PM₁₀ over Europe during the EMEP intensive measurement periods in
745 summer 2012 and winter 2013, *Atmos. Chem. Phys.*, 16, 6107–6129, <https://doi.org/10.5194/acp-16-6107-2016>, 2016.
- 746 Almeida, S. M., Lage, J., Fernández, B., Garcia, S., Reis, M. A., and Chaves, P. C.: Chemical characterization of atmospheric
747 particles and source apportionment in the vicinity of a steelmaking industry, *Science of The Total Environment*, 521–522,
748 411–420, <https://doi.org/10.1016/j.scitotenv.2015.03.112>, 2015.
- 749 Almeida, S. M., Manousakas, M., Diapouli, E., Kertesz, Z., Samek, L., Hristova, E., Šega, K., Alvarez, R. P., Belis, C. A., and
750 Eleftheriadis, K.: Ambient particulate matter source apportionment using receptor modelling in European and Central Asia
751 urban areas, *Environmental Pollution*, 266, 115199, <https://doi.org/10.1016/j.envpol.2020.115199>, 2020.
- 752 Belis, C. A., Cancelinha, J., Duane, M., Forcina, V., Pedroni, V., Passarella, R., Tanet, G., Douglas, K., Piazzalunga, A.,
753 Bolzacchini, E., Sangiorgi, G., Perrone, M.-G., Ferrero, L., Fermo, P., and Larsen, B. R.: Sources for PM air pollution in the
754 Po Plain, Italy: I. Critical comparison of methods for estimating biomass burning contributions to benzo(a)pyrene, *Atmospheric*
755 *Environment*, 45, 7266–7275, <https://doi.org/10.1016/j.atmosenv.2011.08.061>, 2011.
- 756 Belis, C. A., Pernigotti, D., Karagulian, F., Pirovano, G., Larsen, B. R., Gerboles, M., and Hopke, P. K.: A new methodology
757 to assess the performance and uncertainty of source apportionment models in intercomparison exercises, *Atmospheric*
758 *Environment*, 119, 35–44, <https://doi.org/10.1016/j.atmosenv.2015.08.002>, 2015.
- 759 Borlaza, L. J. S., Weber, S., Uzu, G., Jacob, V., Cañete, T., Micallef, S., Trébuchon, C., Slama, R., Favez, O., and Jaffrezo, J.-
760 L.: Disparities in particulate matter (PM₁₀) origins and oxidative potential at a city scale (Grenoble, France) – Part 1: Source
761 apportionment at three neighbouring sites, *Atmos. Chem. Phys.*, 21, 5415–5437, <https://doi.org/10.5194/acp-21-5415-2021>,
762 2021.
- 763 Bougiatioti, A., Stavroulas, I., Kostenidou, E., Zarrmpas, P., Theodosi, C., Kouvarakis, G., Canonaco, F., Prévôt, A. S. H.,
764 Nenes, A., Pandis, S. N., and Mihalopoulos, N.: Processing of biomass-burning aerosol in the eastern Mediterranean during
765 summertime, *Atmos. Chem. Phys.*, 14, 4793–4807, <https://doi.org/10.5194/acp-14-4793-2014>, 2014.

766 Bourtsoukidis, E., Pozzer, A., Williams, J., Makowski, D., Peñuelas, J., Matthaios, V. N., Lazoglou, G., Yañez-Serrano, A.
767 M., Lelieveld, J., Ciais, P., Vrekoussis, M., Daskalakis, N., and Sciare, J.: High temperature sensitivity of monoterpene
768 emissions from global vegetation, *Commun Earth Environ*, 5, 23, <https://doi.org/10.1038/s43247-023-01175-9>, 2024.

769 Bozzetti, C., El Haddad, I., Salameh, D., Daellenbach, K. R., Fermo, P., Gonzalez, R., Minguillón, M. C., Iinuma, Y., Poulain,
770 L., Elser, M., Müller, E., Slowik, J. G., Jaffrezo, J.-L., Baltensperger, U., Marchand, N., and Prévôt, A. S. H.: Organic aerosol
771 source apportionment by offline-AMS over a full year in Marseille, *Atmos. Chem. Phys.*, 17, 8247–8268,
772 <https://doi.org/10.5194/acp-17-8247-2017>, 2017.

773 Brezins, M., Chazeau, B., Marchand, N., Gille, G., Soubise, J., Favez, O., Jaffrezo, J. L., Uzu, G., and D’Anna, B.: Evolution
774 of the V/Ni Ratio in Response to IMO Regulation-Induced Fuel Shifts and Scrubber Use, *Environ. Sci. Technol. Lett.*,
775 <https://doi.org/10.1021/acs.estlett.5c01199>, 2026.

776 Bukowiecki, N., Lienemann, P., Hill, M., Furger, M., Richard, A., Amato, F., Prévôt, A. S. H., Baltensperger, U., Buchmann,
777 B., and Gehrig, R.: PM₁₀ emission factors for non-exhaust particles generated by road traffic in an urban street canyon and
778 along a freeway in Switzerland, *Atmospheric Environment*, 44, 2330–2340, <https://doi.org/10.1016/j.atmosenv.2010.03.039>,
779 2010.

780 Cadeo, L., Biffi, B., Chazeau, B., Colombi, C., Cosenza, R., Cuccia, E., Manousakas, M.-I., Daellenbach, K. R., Prévôt, A. S.
781 H., and Vecchi, R.: Intercomparison of online and offline XRF spectrometers for determining the PM₁₀ elemental composition
782 of ambient aerosol, <https://doi.org/10.5194/egusphere-2025-110>, 11 March 2025.

783 Camman, J., Chazeau, B., Marchand, N., Durand, A., Gille, G., Lanzi, L., Jaffrezo, J.-L., Wortham, H., and Uzu, G.: Oxidative
784 potential apportionment of atmospheric PM₁₀: A new approach combining high-sensitive online analysers for chemical
785 composition and offline OP measurement technique, *Aerosols/Atmospheric Modelling and Data*
786 *Analysis/Troposphere/Chemistry (chemical composition and reactions)*, <https://doi.org/10.5194/egusphere-2023-1441>, 2024.

787 Canonaco, F., Crippa, M., Slowik, J. G., Baltensperger, U., and Prévôt, A. S. H.: SoFi, an IGOR-based interface for the efficient
788 use of the generalized multilinear engine (ME-2) for the source apportionment: ME-2 application to aerosol mass spectrometer
789 data, *Atmos. Meas. Tech.*, 6, 3649–3661, <https://doi.org/10.5194/amt-6-3649-2013>, 2013.

790 Canonaco, F., Tobler, A., Chen, G., Sosedova, Y., Slowik, J. G., Bozzetti, C., Daellenbach, K. R., El Haddad, I., Crippa, M.,
791 Huang, R.-J., Furger, M., Baltensperger, U., and Prévôt, A. S. H.: A new method for long-term source apportionment with
792 time-dependent factor profiles and uncertainty assessment using SoFi Pro: application to 1 year of organic aerosol data, *Atmos.*
793 *Meas. Tech.*, 14, 923–943, <https://doi.org/10.5194/amt-14-923-2021>, 2021.

794 Charron, A., Polo-Rehn, L., Besombes, J.-L., Golly, B., Buisson, C., Chanut, H., Marchand, N., Guillaud, G., and Jaffrezo, J.-
795 L.: Identification and quantification of particulate tracers of exhaust and non-exhaust vehicle emissions, *Atmos. Chem. Phys.*,
796 19, 5187–5207, <https://doi.org/10.5194/acp-19-5187-2019>, 2019.

797 Chazeau, B., Temime-Roussel, B., Gille, G., Mesbah, B., D’Anna, B., Wortham, H., and Marchand, N.: Measurement report:
798 Fourteen months of real-time characterisation of the submicronic aerosol and its atmospheric dynamics at the Marseille–
799 Longchamp supersite, *Atmos. Chem. Phys.*, 21, 7293–7319, <https://doi.org/10.5194/acp-21-7293-2021>, 2021.

800 Chazeau, B., El Haddad, I., Canonaco, F., Temime-Roussel, B., D'Anna, B., Gille, G., Mesbah, B., Prévôt, A. S. H., Wortham,
801 H., and Marchand, N.: Organic aerosol source apportionment by using rolling positive matrix factorization: Application to a
802 Mediterranean coastal city, *Atmospheric Environment: X*, 14, 100176, <https://doi.org/10.1016/j.aeaoa.2022.100176>, 2022.

803 Chebaicheb, H., F. De Brito, J., Chen, G., Tison, E., Marchand, C., Prévôt, A. S. H., Favez, O., and Riffault, V.: Investigation
804 of four-year chemical composition and organic aerosol sources of submicron particles at the ATOLL site in northern France,
805 *Environmental Pollution*, 330, 121805, <https://doi.org/10.1016/j.envpol.2023.121805>, 2023.

806 Chen, G., Sosedova, Y., Canonaco, F., Fröhlich, R., Tobler, A., Vlachou, A., Daellenbach, K. R., Bozzetti, C., Hueglin, C.,
807 Graf, P., Baltensperger, U., Slowik, J. G., El Haddad, I., and Prévôt, A. S. H.: Time-dependent source apportionment of
808 submicron organic aerosol for a rural site in an alpine valley using a rolling positive matrix factorisation (PMF) window,
809 *Atmos. Chem. Phys.*, 21, 15081–15101, <https://doi.org/10.5194/acp-21-15081-2021>, 2021.

810 Chen, G., Canonaco, F., Tobler, A., Aas, W., Alastuey, A., Allan, J., Atabakhsh, S., Aurela, M., Baltensperger, U., Bougiatioti,
811 A., De Brito, J. F., Ceburnis, D., Chazeau, B., Chebaicheb, H., Daellenbach, K. R., Ehn, M., El Haddad, I., Eleftheriadis, K.,
812 Favez, O., Flentje, H., Font, A., Fossum, K., Freney, E., Gini, M., Green, D. C., Heikkinen, L., Herrmann, H., Kalogridis, A.-
813 C., Keernik, H., Lhotka, R., Lin, C., Lunder, C., Maasikmets, M., Manousakas, M. I., Marchand, N., Marin, C., Marmureanu,
814 L., Mihalopoulos, N., Močnik, G., Nęcki, J., O'Dowd, C., Ovadnevaite, J., Peter, T., Petit, J.-E., Pikridas, M., Matthew Platt,
815 S., Pokorná, P., Poulain, L., Priestman, M., Riffault, V., Rinaldi, M., Rózański, K., Schwarz, J., Sciare, J., Simon, L., Skiba,
816 A., Slowik, J. G., Sosedova, Y., Stavroulas, I., Styszko, K., Teinmaa, E., Timonen, H., Tremper, A., Vasilescu, J., Via, M.,
817 Vodička, P., Wiedensohler, A., Zografou, O., Cruz Minguillón, M., and Prévôt, A. S. H.: European aerosol phenomenology –
818 8: Harmonised source apportionment of organic aerosol using 22 Year-long ACSM/AMS datasets, *Environment International*,
819 166, 107325, <https://doi.org/10.1016/j.envint.2022.107325>, 2022a.

820 Chen, G., Canonaco, F., Slowik, J. G., Daellenbach, K. R., Tobler, A., Petit, J.-E., Favez, O., Stavroulas, I., Mihalopoulos, N.,
821 Gerasopoulos, E., El Haddad, I., Baltensperger, U., and Prévôt, A. S. H.: Real-Time Source Apportionment of Organic
822 Aerosols in Three European Cities, *Environ. Sci. Technol.*, 56, 15290–15297, <https://doi.org/10.1021/acs.est.2c02509>, 2022b.

823 Chevet, E., Boiron, O., and Anselmet, F.: Modeling of air pollution due to marine traffic in Marseille, *Atmospheric*
824 *Environment*, 329, 120542, <https://doi.org/10.1016/j.atmosenv.2024.120542>, 2024.

825 Clements, N., Eav, J., Xie, M., Hannigan, M. P., Miller, S. L., Navidi, W., Peel, J. L., Schauer, J. J., Shafer, M. M., and Milford,
826 J. B.: Concentrations and source insights for trace elements in fine and coarse particulate matter, *Atmospheric Environment*,
827 89, 373–381, <https://doi.org/10.1016/j.atmosenv.2014.01.011>, 2014.

828 Dall'Osto, M., Querol, X., Amato, F., Karanasiou, A., Lucarelli, F., Nava, S., Calzolari, G., and Chiari, M.: Hourly elemental
829 concentrations in PM_{2.5}; aerosols sampled simultaneously at urban background and road site during
830 SAPUSS – diurnal variations and PMF receptor modelling, *Atmos. Chem. Phys.*, 13, 4375–4392, [https://doi.org/10.5194/acp-](https://doi.org/10.5194/acp-13-4375-2013)
831 [13-4375-2013](https://doi.org/10.5194/acp-13-4375-2013), 2013.

832 Dockery DW, Pope CA 3rd, Xu X, Spengler JD, Ware JH, Fay ME, Ferris BG Jr, Speizer FE. An association between air
833 pollution and mortality in six U.S. cities. *N Engl J Med.* 1993 Dec 9;329(24):1753-9. doi: 10.1056/NEJM199312093292401.
834 PMID: 8179653.

835 Ding, X., Li, Q., Wu, D., Huo, Y., Liang, Y., Wang, H., Zhang, J., Wang, S., Wang, T., Ye, X., and Chen, J.: Gaseous and
836 Particulate Chlorine Emissions From Typical Iron and Steel Industry in China, *JGR Atmospheres*, 125, e2020JD032729,
837 <https://doi.org/10.1029/2020JD032729>, 2020.

838 Drinovec, L., Močnik, G., Zotter, P., Prévôt, A. S. H., Ruckstuhl, C., Coz, E., Rupakheti, M., Sciare, J., Müller, T.,
839 Wiedensohler, A., and Hansen, A. D. A.: The “dual-spot” Aethalometer: an improved measurement of aerosol
840 black carbon with real-time loading compensation, *Atmos. Meas. Tech.*, 8, 1965–1979, [https://doi.org/10.5194/amt-8-1965-](https://doi.org/10.5194/amt-8-1965-2015)
841 [2015](https://doi.org/10.5194/amt-8-1965-2015), 2015.

842 Drobinski, P., Saïd, F., Ancellet, G., Arteta, J., Augustin, P., Bastin, S., Brut, A., Caccia, J. L., Campistron, B., Cautenet, S.,
843 Colette, A., Coll, I., Corsmeier, U., Cros, B., Dabas, A., Delbarre, H., Dufour, A., Durand, P., Guénard, V., Hasel, M., Kalthoff,
844 N., Kottmeier, C., Lasry, F., Lemonsu, A., Lohou, F., Masson, V., Menut, L., Moppert, C., Peuch, V. H., Puygrenier, V.,
845 Reitebuch, O., and Vautard, R.: Regional transport and dilution during high-pollution episodes in southern France: Summary
846 of findings from the Field Experiment to Constraint Models of Atmospheric Pollution and Emissions Transport (ESCOMPTE),
847 *J. Geophys. Res.*, 112, 2006JD007494, <https://doi.org/10.1029/2006JD007494>, 2007.

848 Dubois, N., Foret, G., Siour, G., Uzu, G., Couvidat, F., Vida, M., André, J.-M., Moukhtar, S., Sirina-Leboine, N., Aujay-
849 Plouzeau, R., Alleman, L., Conil, S., Pallares, C., Salque-Moreton, G., Stratigou, E., Alastuey, A., Querol, X., Ito, A., Jaffrezo,
850 J.-L., Favez, O., and Beekmann, M.: Construction of copper, iron and manganese anthropogenic emission inventories for
851 Europe, *Atmospheric Environment*, 363, 121582, <https://doi.org/10.1016/j.atmosenv.2025.121582>, 2025.

852 Dufresne, M., Salameh, T., Leonardis, T., Gille, G., Armengaud, A., and Sauvage, S.: Volatile organic compound sources and
853 impacts in an urban Mediterranean area (Marseille, France), *Atmos. Chem. Phys.*, 25, 5977–5999, [https://doi.org/10.5194/acp-](https://doi.org/10.5194/acp-25-5977-2025)
854 [25-5977-2025](https://doi.org/10.5194/acp-25-5977-2025), 2025.

855 Efron, B. “Bootstrap Methods: Another Look at the Jackknife.” *The Annals of Statistics*, vol. 7, no. 1, pp. 1–26. JSTOR,
856 <http://www.jstor.org/stable/2958830>, 1979.

857 El Haddad, I., Marchand, N., Temime-Roussel, B., Wortham, H., Piot, C., Besombes, J.-L., Baduel, C., Voisin, D., Armengaud,
858 A., and Jaffrezo, J.-L.: Insights into the secondary fraction of the organic aerosol in a Mediterranean urban area: Marseille,
859 *Atmos. Chem. Phys.*, 11, 2059–2079, <https://doi.org/10.5194/acp-11-2059-2011>, 2011.

860 El Haddad, I., D’Anna, B., Temime-Roussel, B., Nicolas, M., Boreave, A., Favez, O., Voisin, D., Sciare, J., George, C.,
861 Jaffrezo, J.-L., Wortham, H., and Marchand, N.: Towards a better understanding of the origins, chemical composition and
862 aging of oxygenated organic aerosols: case study of a Mediterranean industrialized environment, Marseille, *Atmos. Chem.*
863 *Phys.*, 13, 7875–7894, <https://doi.org/10.5194/acp-13-7875-2013>, 2013.

864 Eldred, R. A.: Comparison of Selenium and Sulfur at Remote Sites, *Journal of the Air & Waste Management Association*, 47,
865 204–211, <https://doi.org/10.1080/10473289.1997.10464423>, 1997.

866 Enestam, S., Boman, C., Niemi, J., Boström, D., Backman, R., Mäkelä, K., and Hupa, M.: Occurrence of Zinc and Lead in
867 Aerosols and Deposits in the Fluidized-Bed Combustion of Recovered Waste Wood. Part 1: Samples from Boilers, Energy
868 Fuels, 25, 1396–1404, <https://doi.org/10.1021/ef101478n>, 2011.

869 European Commission. Joint Research Centre. Institute for Environment and Sustainability: The Krakow receptor modelling
870 inter-comparison exercise, Publications Office, LU, 2008.

871 Faxon, C., Bean, J., and Ruiz, L.: Inland Concentrations of Cl₂ and ClNO₂ in Southeast Texas Suggest Chlorine Chemistry
872 Significantly Contributes to Atmospheric Reactivity, Atmosphere, 6, 1487–1506, <https://doi.org/10.3390/atmos6101487>,
873 2015.

874 Flaounas, E., Coll, I., Armengaud, A., and Schmechtig, C.: The representation of dust transport and missing urban sources as
875 major issues for the simulation of PM episodes in a Mediterranean area, Atmos. Chem. Phys., 2009.

876 Formenti, P., Nava, S., Prati, P., Chevaillier, S., Klaver, A., Lafon, S., Mazzei, F., Calzolari, G., and Chiari, M.: Self-attenuation
877 artifacts and correction factors of light element measurements by X-ray analysis: Implication for mineral dust composition
878 studies, J. Geophys. Res., 115, 2009JD012701, <https://doi.org/10.1029/2009JD012701>, 2010.

879 Fossum, K. N., Lin, C., O’Sullivan, N., Lei, L., Hellebust, S., Ceburnis, D., Afzal, A., Tremper, A., Green, D., Jain, S.,
880 Byčenkienė, S., O’Dowd, C., Wenger, J., and Ovadnevaite, J.: Two distinct ship emission profiles for organic-sulfate source
881 apportionment of PM in sulfur emission control areas, Atmos. Chem. Phys., 24, 10815–10831, [https://doi.org/10.5194/acp-](https://doi.org/10.5194/acp-24-10815-2024)
882 [24-10815-2024](https://doi.org/10.5194/acp-24-10815-2024), 2024.

883 Fröhlich, R., Cubison, M. J., Slowik, J. G., Bukowiecki, N., Prévôt, A. S. H., Baltensperger, U., Schneider, J., Kimmel, J. R.,
884 Gonin, M., Rohner, U., Worsnop, D. R., and Jayne, J. T.: The ToF-ACSM: a portable aerosol chemical speciation monitor
885 with TOFMS detection, Atmos. Meas. Tech., 6, 3225–3241, <https://doi.org/10.5194/amt-6-3225-2013>, 2013.

886 Fuller, R., Landrigan, P. J., Balakrishnan, K., Bathan, G., Bose-O’Reilly, S., Brauer, M., Caravanos, J., Chiles, T., Cohen, A.,
887 Corra, L., Cropper, M., Ferraro, G., Hanna, J., Hanrahan, D., Hu, H., Hunter, D., Janata, G., Kupka, R., Lanphear, B., Lichtveld,
888 M., Martin, K., Mustapha, A., Sanchez-Triana, E., Sandilya, K., Schaefli, L., Shaw, J., Seddon, J., Suk, W., Téllez-Rojo, M.
889 M., and Yan, C.: Pollution and health: a progress update, The Lancet Planetary Health, 6, e535–e547,
890 [https://doi.org/10.1016/S2542-5196\(22\)00090-0](https://doi.org/10.1016/S2542-5196(22)00090-0), 2022.

891 Furger, M., Minguillón, M. C., Yadav, V., Slowik, J. G., Hüglin, C., Fröhlich, R., Petterson, K., Baltensperger, U., and Prévôt,
892 A. S. H.: Elemental composition of ambient aerosols measured with high temporal resolution using an online XRF
893 spectrometer, Atmos. Meas. Tech., 10, 2061–2076, <https://doi.org/10.5194/amt-10-2061-2017>, 2017.

894 Gomes, L., Bergametti, G., Coudé-Gaussen, G., and Rognon, P.: Submicron desert dusts: A sandblasting process, J. Geophys.
895 Res., 95, 13927–13935, <https://doi.org/10.1029/JD095iD09p13927>, 1990.

896 Gomez, J., Allen, R. J., Turnock, S. T., Horowitz, L. W., Tsigaridis, K., Bauer, S. E., Olivié, D., Thomson, E. S., and Ginoux,
897 P.: The projected future degradation in air quality is caused by more abundant natural aerosols in a warmer world, Commun
898 Earth Environ, 4, 22, <https://doi.org/10.1038/s43247-023-00688-7>, 2023.

899 Guo, Z., Wang, Q., Chen, N., Zhu, B., Zheng, H., Kong, S., Xie, M., and Yu, H.: Source Apportionment of Fine Particulate
900 Matter in Wuhan: Application of Rolling Positive Matrix Factorization Under Different Seasons and Episodic Events, *Aerosol*
901 *Air Qual. Res.*, 25, 7, <https://doi.org/10.1007/s44408-025-00005-1>, 2025.

902 Heikkinen, L., Äijälä, M., Daellenbach, K. R., Chen, G., Garmash, O., Aliaga, D., Graeffe, F., Rätty, M., Luoma, K., Aalto, P.,
903 Kulmala, M., Petäjä, T., Worsnop, D., and Ehn, M.: Eight years of sub-micrometre organic aerosol composition data from the
904 boreal forest characterized using a machine-learning approach, *Atmos. Chem. Phys.*, 21, 10081–10109,
905 <https://doi.org/10.5194/acp-21-10081-2021>, 2021.

906 Janhall, S., Andreae, M. O., and Poschl, U.: Biomass burning aerosol emissions from vegetation fires: particle number and
907 mass emission factors and size distributions, *Atmos. Chem. Phys.*, 2010.

908 Jeanjean, M., Dron, J., Allen, B. L., Gramaglia, C., Austruy, A., Lees, J., Ferrier, Y., Periot, M., Dotson, M. P., Chamaret, P.,
909 and Cohen, A. K.: Participatory environmental health research: A tool to explore the socio-exposome in a major european
910 industrial zone, *Environmental Research*, 218, 114865, <https://doi.org/10.1016/j.envres.2022.114865>, 2023.

911 Jézéquel, A., Faranda, D., Drobinski, P., and Lionello, P.: Extreme Event Attribution in the Mediterranean, *Intl Journal of*
912 *Climatology*, e8799, <https://doi.org/10.1002/joc.8799>, 2025.

913 Jonsson, Å. M., Westerlund, J., and Hallquist, M.: Size-resolved particle emission factors for individual ships: PARTICLE
914 EFs FROM INDIVIDUAL SHIPS, *Geophys. Res. Lett.*, 38, n/a-n/a, <https://doi.org/10.1029/2011GL047672>, 2011.

915 Jordan, C. E., Pszenny, A. A. P., Keene, W. C., Cooper, O. R., Deegan, B., Maben, J., Routhier, M., Sander, R., and Young,
916 A. H.: Origins of aerosol chlorine during winter over north central Colorado, USA, *JGR Atmospheres*, 120, 678–694,
917 <https://doi.org/10.1002/2014JD022294>, 2015.

918 Keene, William C., Khalil, M. A. K., Erickson, David J., McCulloch, A., Graedel, T. E., Lobert, J. M., Aucott, M. L., Gong,
919 S. L., Harper, D. B., Kleiman, G., Midgley, P., Moore, R. M., Seuzaret, C., Sturges, W. T., Benkovitz, C. M., Koropalov, V.,
920 Barrie, L. A., and Li, Y. F.: Composite global emissions of reactive chlorine from anthropogenic and natural sources: Reactive
921 Chlorine Emissions Inventory, *J. Geophys. Res.*, 104, 8429–8440, <https://doi.org/10.1029/1998JD100084>, 1999.

922 Kfoury, A., Ledoux, F., Roche, C., Delmaire, G., Roussel, G., and Courcot, D.: PM_{2.5} source apportionment in a French urban
923 coastal site under steelworks emission influences using constrained non-negative matrix factorization receptor model, *Journal*
924 *of Environmental Sciences*, 40, 114–128, <https://doi.org/10.1016/j.jes.2015.10.025>, 2016.

925 Kothai, P., Saradhi, I. V., Pandit, G. G., Markwitz, A., and Puranik, V. D.: Chemical Characterization and Source Identification
926 of Particulate Matter at an Urban Site of Navi Mumbai, India, *Aerosol Air Qual. Res.*, 11, 560–569,
927 <https://doi.org/10.4209/aaqr.2011.02.0017>, 2011.

928 Kreyling, W. G., Semmler-Behnke, M., and Möller, W.: Ultrafine Particle–Lung Interactions: Does Size Matter?, *Journal of*
929 *Aerosol Medicine*, 19, 74–83, <https://doi.org/10.1089/jam.2006.19.74>, 2006.

930 Kuittinen, N., Timonen, H., Karjalainen, P., Murtonen, T., Vesala, H., Bloss, M., Honkanen, M., Lehtoranta, K., Aakko-Saksa,
931 P., and Rönkkö, T.: In-depth characterization of exhaust particles performed on-board a modern cruise ship applying a
932 scrubber, *Science of The Total Environment*, 946, 174052, <https://doi.org/10.1016/j.scitotenv.2024.174052>, 2024.

933 Kumar, S., Aggarwal, S. G., Gupta, P. K., and Kawamura, K.: Investigation of the tracers for plastic-enriched waste burning
934 aerosols, *Atmospheric Environment*, 108, 49–58, <https://doi.org/10.1016/j.atmosenv.2015.02.066>, 2015.

935 Kumar, V., Sahu, M., Biswal, B., Prakash, J., Choudhary, S., Raliya, R., Chadha, T. S., Fang, J., and Biswas, P.: Temporal
936 dynamics and source characteristics of fine particulate matter using Positive Matrix Factorization (PMF), *Atmospheric*
937 *Pollution Research*, 16, 102539, <https://doi.org/10.1016/j.apr.2025.102539>, 2025.

938 Lack, D. A., Moosmüller, H., McMeeking, G. R., Chakrabarty, R. K., and Baumgardner, D.: Characterizing elemental,
939 equivalent black, and refractory black carbon aerosol particles: a review of techniques, their limitations and uncertainties, *Anal*
940 *Bioanal Chem*, 406, 99–122, <https://doi.org/10.1007/s00216-013-7402-3>, 2014.

941 Larssen, S., Sluyter, R., and Helmis, C.: Criteria for EUROAIRNET - The EEA Air Quality Monitoring and Information
942 Network, n.d.

943 Le Berre, L., Temime-Roussel, B., Lanzafame, G. M., D'Anna, B., Marchand, N., Sauvage, S., Dufresne, M., Tinel, L.,
944 Leonardis, T., Ferreira De Brito, J., Armengaud, A., Gille, G., Lanzi, L., Bourjot, R., and Wortham, H.: Measurement report:
945 In-depth characterization of ship emissions during operations in a Mediterranean port, [https://doi.org/10.5194/egusphere-2024-](https://doi.org/10.5194/egusphere-2024-2903)
946 [2903](https://doi.org/10.5194/egusphere-2024-2903), 25 September 2024.

947 Le Breton, M., Hallquist, Å. M., Pathak, R. K., Simpson, D., Wang, Y., Johansson, J., Zheng, J., Yang, Y., Shang, D., Wang,
948 H., Liu, Q., Chan, C., Wang, T., Bannan, T. J., Priestley, M., Percival, C. J., Shallcross, D. E., Lu, K., Guo, S., Hu, M., and
949 Hallquist, M.: Chlorine oxidation of VOCs at a semi-rural site in Beijing: significant chlorine liberation from
950 CINO₂ and subsequent gas- and particle-phase Cl–VOC production, *Atmos. Chem. Phys.*, 18, 13013–
951 13030, <https://doi.org/10.5194/acp-18-13013-2018>, 2018.

952 Ledoux, F., Laversin, H., Courcot, D., Courcot, L., Zhilinskaya, E. A., Puskaric, E., and Aboukaïs, A.: Characterization of iron
953 and manganese species in atmospheric aerosols from anthropogenic sources, *Atmospheric Research*, 82, 622–632,
954 <https://doi.org/10.1016/j.atmosres.2006.02.018>, 2006.

955 Lee, B. H., Lopez-Hilfiker, F. D., Schroder, J. C., Campuzano-Jost, P., Jimenez, J. L., McDuffie, E. E., Fibiger, D. L., Veres,
956 P. R., Brown, S. S., Campos, T. L., Weinheimer, A. J., Flocke, F. F., Norris, G., O'Mara, K., Green, J. R., Fiddler, M. N.,
957 Bililign, S., Shah, V., Jaeglé, L., and Thornton, J. A.: Airborne Observations of Reactive Inorganic Chlorine and Bromine
958 Species in the Exhaust of Coal-Fired Power Plants, *JGR Atmospheres*, 123, <https://doi.org/10.1029/2018JD029284>, 2018.

959 Lei, L., Xu, W., Lin, C., Chen, B., Fossum, K. N., Ceburnis, D., O'Dowd, C., and Ovadnevaite, J.: Enhancing Differentiation
960 of Oxygenated Organic Aerosol: A Machine Learning Approach to Distinguish Local and Transboundary Pollution, *ACS EST*
961 *Air*, 2, 891–902, <https://doi.org/10.1021/acsestair.4c00331>, 2025.

962 Lin, C., Ceburnis, D., O'Dowd, C., and Ovadnevaite, J.: Seasonality of Aerosol Sources Calls for Distinct Air Quality
963 Mitigation Strategies, *Toxics*, 10, 121, <https://doi.org/10.3390/toxics10030121>, 2022.

964 Liu, T., Chan, A. W. H., and Abbatt, J. P. D.: Multiphase Oxidation of Sulfur Dioxide in Aerosol Particles: Implications for
965 Sulfate Formation in Polluted Environments, *Environ. Sci. Technol.*, 55, 4227–4242, <https://doi.org/10.1021/acs.est.0c06496>,
966 2021.

967 Liu, X., Zhang, X., Jin, B., Wang, T., Qian, S., Zou, J., Dinh, V. N. T., Jaffrezo, J.-L., Uzu, G., Dominutti, P., Darfeuil, S.,
968 Favez, O., Conil, S., Marchand, N., Castillo, S., De La Rosa, J. D., Grange, S., Hueglin, C., Eleftheriadis, K., Diapouli, E.,
969 Manousakas, M.-I., Gini, M., Nava, S., Calzolari, G., Alves, C., Monge, M., Reche, C., Harrison, R. M., Hopke, P. K., Alastuey,
970 A., and Querol, X.: Source apportionment of PM₁₀ based on offline chemical speciation data at 24 European sites, *npj Clim*
971 *Atmos Sci*, 8, <https://doi.org/10.1038/s41612-025-01097-7>, 2025.

972 Lu, G., Brook, J. R., Rami Alfarra, M., Anlauf, K., Richard Leaitch, W., Sharma, S., Wang, D., Worsnop, D. R., and Phinney,
973 L.: Identification and characterization of inland ship plumes over Vancouver, BC, *Atmospheric Environment*, 40, 2767–2782,
974 <https://doi.org/10.1016/j.atmosenv.2005.12.054>, 2006.

975 Manousakas, M., Furger, M., Daellenbach, K. R., Canonaco, F., Chen, G., Tobler, A., Rai, P., Qi, L., Tremper, A. H., Green,
976 D., Hueglin, C., Slowik, J. G., El Haddad, I., and Prevot, A. S. H.: Source identification of the elemental fraction of particulate
977 matter using size segregated, highly time-resolved data and an optimized source apportionment approach, *Atmospheric*
978 *Environment: X*, 14, 100165, <https://doi.org/10.1016/j.aeaoa.2022.100165>, 2022.

979 Manousakas, M. I., Zografou, O., Canonaco, F., Diapouli, E., Papagiannis, S., Gini, M., Vasilatou, V., Tobler, A., Vratolis, S.,
980 Slowik, J. G., Daellenbach, K. R., Prevot, A. S. H., and Eleftheriadis, K.: Implementation of Real-Time Source Apportionment
981 Approaches Using the ACSM-Xact-Aethalometer (AXA) Set-Up with SoFi RT: The Athens Case Study,
982 <https://doi.org/10.5194/egusphere-2025-542>, 24 February 2025.

983 Marris, H., Deboudt, K., Augustin, P., Flament, P., Blond, F., Fiani, E., Fourmentin, M., and Delbarre, H.: Fast changes in
984 chemical composition and size distribution of fine particles during the near-field transport of industrial plumes, *Science of The*
985 *Total Environment*, 427–428, 126–138, <https://doi.org/10.1016/j.scitotenv.2012.03.068>, 2012.

986 Masoud, C. G., Modi, M., Bhattacharyya, N., Jahn, L. G., McPherson, K. N., Abue, P., Patel, K., Allen, D. T., and Hildebrandt
987 Ruiz, L.: High Chlorine Concentrations in an Unconventional Oil and Gas Development Region and Impacts on Atmospheric
988 Chemistry, *Environ. Sci. Technol.*, 57, 15454–15464, <https://doi.org/10.1021/acs.est.3c04005>, 2023.

989 Massimi, L., Simonetti, G., Buiarelli, F., Di Filippo, P., Pomata, D., Riccardi, C., Ristorini, M., Astolfi, M. L., and Canepari,
990 S.: Spatial distribution of levoglucosan and alternative biomass burning tracers in atmospheric aerosols, in an urban and
991 industrial hot-spot of Central Italy, *Atmospheric Research*, 239, 104904, <https://doi.org/10.1016/j.atmosres.2020.104904>,
992 2020.

993 Moffet, R. C., Desyaterik, Y., Hopkins, R. J., Tivanski, A. V., Gilles, M. K., Wang, Y., Shutthanandan, V., Molina, L. T.,
994 Abraham, R. G., Johnson, K. S., Mugica, V., Molina, M. J., Laskin, A., and Prather, K. A.: Characterization of Aerosols
995 Containing Zn, Pb, and Cl from an Industrial Region of Mexico City, *Environ. Sci. Technol.*, 42, 7091–7097,
996 <https://doi.org/10.1021/es7030483>, 2008.

997 Momenimovahed, A., Gagné, S., Gajdosechova, Z., Corbin, J. C., Smallwood, G. J., Mester, Z., Behrends, B., Wichmann, V.,
998 and Thomson, K. A.: Effective density and metals content of particle emissions generated by a diesel engine operating under
999 different marine fuels, *Journal of Aerosol Science*, 151, 105651, <https://doi.org/10.1016/j.jaerosci.2020.105651>, 2021.

1000 Morais, S., Fonseca, H. M. A. C., Oliveira, S. M. R., Oliveira, H., Gupta, V. K., Sharma, B., and De Lourdes Pereira, M.:
1001 Environmental and Health Hazards of Chromated Copper Arsenate-Treated Wood: A Review, *IJERPH*, 18, 5518,
1002 <https://doi.org/10.3390/ijerph18115518>, 2021.

1003 Moreno, T., Pandolfi, M., Querol, X., Lavín, J., Alastuey, A., Viana, M., and Gibbons, W.: Manganese in the urban atmosphere:
1004 identifying anomalous concentrations and sources, *Environ Sci Pollut Res*, 18, 173–183, [https://doi.org/10.1007/s11356-010-](https://doi.org/10.1007/s11356-010-0353-8)
1005 [0353-8](https://doi.org/10.1007/s11356-010-0353-8), 2011.

1006 Ngoc Thuy Dinh, V., Jaffrezo, J.-L., Dominutti, P., Elazzouzi, R., Darfeuil, S., Voiron, C., Marsal, A., Socquet, S., Mary, G.,
1007 Cozic, J., Coulaud, C., Durif, M., Favez, O., and Uzu, G.: Decadal trends (2013–2023) in PM10 sources and oxidative potential
1008 at a European urban supersite (Alpine Valley, Grenoble, France), <https://doi.org/10.5194/egusphere-2025-2933>, 1 July 2025.

1009 Paatero, P.: The Multilinear Engine: A Table-Driven, Least Squares Program for Solving Multilinear Problems, including the
1010 n-Way Parallel Factor Analysis Model, 2024.

1011 Paatero, P. and Hopke, P. K.: Discarding or downweighting high-noise variables in factor analytic models, *Analytica Chimica*
1012 *Acta*, 490, 277–289, [https://doi.org/10.1016/S0003-2670\(02\)01643-4](https://doi.org/10.1016/S0003-2670(02)01643-4), 2003.

1013 Paatero, P. and Hopke, P. K.: Rotational tools for factor analytic models, *Journal of Chemometrics*, 23, 91–100,
1014 <https://doi.org/10.1002/cem.1197>, 2009.

1015 Paatero, P. and Tapper, U.: Positive matrix factorization: A non-negative factor model with optimal utilization of error
1016 estimates of data values, *Environmetrics*, 5, 111–126, <https://doi.org/10.1002/env.3170050203>, 1994.

1017 Pant, P., Shi, Z., Pope, F. D., and Harrison, R. M.: Characterization of Traffic-Related Particulate Matter Emissions in a Road
1018 Tunnel in Birmingham, UK: Trace Metals and Organic Molecular Markers, *Aerosol Air Qual. Res.*, 17, 117–130,
1019 <https://doi.org/10.4209/aaqr.2016.01.0040>, 2017.

1020 Parworth, C., Fast, J., Mei, F., Shippert, T., Sivaraman, C., Tilp, A., Watson, T., and Zhang, Q.: Long-term measurements of
1021 submicrometer aerosol chemistry at the Southern Great Plains (SGP) using an Aerosol Chemical Speciation Monitor (ACSM),
1022 *Atmospheric Environment*, 106, 43–55, <https://doi.org/10.1016/j.atmosenv.2015.01.060>, 2015.

1023 Pawar, P. V., Ghude, S. D., Govardhan, G., Acharja, P., Kulkarni, R., Kumar, R., Sinha, B., Sinha,
1024 V., Jena, C., Gunwani, P., Adhya, T. K., Nemitz, E., and Sutton, M. A.: Chloride (HCl / Cl⁻) dominates
1025 inorganic aerosol formation from ammonia in the Indo-Gangetic Plain during winter: modeling and comparison with
1026 observations, *Atmos. Chem. Phys.*, 23, 41–59, <https://doi.org/10.5194/acp-23-41-2023>, 2023.

1027 Peng, X., Wang, W., Xia, M., Chen, H., Ravishankara, A. R., Li, Q., Saiz-Lopez, A., Liu, P., Zhang, F., Zhang, C., Xue, L.,
1028 Wang, X., George, C., Wang, J., Mu, Y., Chen, J., and Wang, T.: An unexpected large continental source of reactive bromine
1029 and chlorine with significant impact on wintertime air quality, *National Science Review*, 8, nwaa304,
1030 <https://doi.org/10.1093/nsr/nwaa304>, 2021.

1031 Pernigotti, D. and Belis, C. A.: DeltaSA tool for source apportionment benchmarking, description and sensitivity analysis,
1032 *Atmospheric Environment*, 180, 138–148, <https://doi.org/10.1016/j.atmosenv.2018.02.046>, 2018.

1033 Pey, J., Pérez, N., Castillo, S., Viana, M., Moreno, T., Pandolfi, M., López-Sebastián, J. M., Alastuey, A., and Querol, X.:
1034 Geochemistry of regional background aerosols in the Western Mediterranean, *Atmospheric Research*, 94, 422–435,
1035 <https://doi.org/10.1016/j.atmosres.2009.07.001>, 2009.

1036 Pey, J., Alastuey, A., and Querol, X.: PM₁₀ and PM_{2.5} sources at an insular location in the western Mediterranean by using
1037 source apportionment techniques, *Science of The Total Environment*, 456–457, 267–277,
1038 <https://doi.org/10.1016/j.scitotenv.2013.03.084>, 2013.

1039 Polissar, A. V., Hopke, P. K., Paatero, P., Malm, W. C., and Sisler, J. F.: Atmospheric aerosol over Alaska: 2. Elemental
1040 composition and sources, *J. Geophys. Res.*, 103, 19045–19057, <https://doi.org/10.1029/98JD01212>, 1998.

1041 Pons, F., Alberti, T., Messori, G., Dulac, F., and Faranda, D.: Assessing Climate Change Impacts on the March 2024
1042 Compound Floods and Saharan Dust Outbreak in Europe, *JGR Atmospheres*, 130, e2024JD042218,
1043 <https://doi.org/10.1029/2024JD042218>, 2025.

1044 Puygrenier, V., Lohou, F., Campistron, B., Saïd, F., Pigeon, G., Bénech, B., and Serça, D.: Investigation on the fine structure
1045 of sea-breeze during ESCOMPTE experiment, *Atmospheric Research*, 74, 329–353,
1046 <https://doi.org/10.1016/j.atmosres.2004.06.011>, 2005.

1047 Quivet, E., Höhener, P., Temime-Roussel, B., Dron, J., Revenko, G., Verlande, M., Lebaron, K., Demelas, C., Vassalo, L.,
1048 and Boudenne, J.-L.: Underestimation of Anthropogenic Bromoform Released into the Environment?, *Environ. Sci. Technol.*,
1049 56, 1522–1533, <https://doi.org/10.1021/acs.est.1c05073>, 2022.

1050 Rai, P., Furger, M., El Haddad, I., Kumar, V., Wang, L., Singh, A., Dixit, K., Bhattu, D., Petit, J.-E., Ganguly, D., Rastogi, N.,
1051 Baltensperger, U., Tripathi, S. N., Slowik, J. G., and Prévôt, A. S. H.: Real-time measurement and source apportionment of
1052 elements in Delhi's atmosphere, *Science of The Total Environment*, 742, 140332,
1053 <https://doi.org/10.1016/j.scitotenv.2020.140332>, 2020a.

1054 Rai, P., Furger, M., Slowik, J. G., Canonaco, F., Fröhlich, R., Hüglin, C., Minguillón, M. C., Petterson, K., Baltensperger, U.,
1055 and Prévôt, A. S. H.: Source apportionment of highly time-resolved elements during a firework episode from a rural freeway
1056 site in Switzerland, *Atmospheric Chemistry and Physics*, 20, 1657–1674, <https://doi.org/10.5194/acp-20-1657-2020>, 2020b.

1057 Rai, P., Furger, M., Slowik, J. G., Zhong, H., Tong, Y., Wang, L., Duan, J., Gu, Y., Qi, L., Huang, R.-J., Cao, J., Baltensperger,
1058 U., and Prévôt, A. S. H.: Characteristics and sources of hourly elements in PM₁₀ and PM_{2.5} during wintertime in Beijing,
1059 *Environmental Pollution*, 278, 116865, <https://doi.org/10.1016/j.envpol.2021.116865>, 2021.

1060 Reff, A., Eberly, S. I., and Bhave, P. V.: Receptor Modeling of Ambient Particulate Matter Data Using Positive Matrix
1061 Factorization: Review of Existing Methods, *Journal of the Air & Waste Management Association*, 57, 146–154,
1062 <https://doi.org/10.1080/10473289.2007.10465319>, 2007.

1063 Riandet, A., Xueref-Remy, I., Popovici, I., Lelandais, L., Armengaud, A., and Goloub, P.: Diurnal and Seasonal Variability of
1064 the Atmospheric Boundary-Layer Height in Marseille (France) for Mistral and Sea/Land Breeze Conditions, *Remote Sensing*,
1065 15, 1185, <https://doi.org/10.3390/rs15051185>, 2023.

1066 Riffault, V., Arndt, J., Marris, H., Mbengue, S., Setyan, A., Alleman, L. Y., Deboudt, K., Flament, P., Augustin, P., Delbarre,
1067 H., and Wenger, J.: Fine and Ultrafine Particles in the Vicinity of Industrial Activities: A Review, *Critical Reviews in*
1068 *Environmental Science and Technology*, 45, 2305–2356, <https://doi.org/10.1080/10643389.2015.1025636>, 2015.

1069 Roy, P.-O., Bulle, C., and Deschênes, L.: Global-scale atmospheric modeling of aerosols to assess metal source-receptor
1070 relationships for life cycle assessment, *Int J Life Cycle Assess*, 24, 93–103, <https://doi.org/10.1007/s11367-018-1508-y>, 2019.

1071 Salameh, D., Detournay, A., Pey, J., Pérez, N., Liguori, F., Saraga, D., Bove, M. C., Brotto, P., Cassola, F., Massabò, D.,
1072 Latella, A., Pillon, S., Formenton, G., Patti, S., Armengaud, A., Piga, D., Jaffrezo, J. L., Bartzis, J., Tolis, E., Prati, P., Querol,
1073 X., Wortham, H., and Marchand, N.: PM_{2.5} chemical composition in five European Mediterranean cities: A 1-year study,
1074 *Atmospheric Research*, 155, 102–117, <https://doi.org/10.1016/j.atmosres.2014.12.001>, 2015.

1075 Salameh, D., Pey, J., Bozzetti, C., El Haddad, I., Detournay, A., Sylvestre, A., Canonaco, F., Armengaud, A., Piga, D., Robin,
1076 D., Prevot, A. S. H., Jaffrezo, J.-L., Wortham, H., and Marchand, N.: Sources of PM_{2.5} at an urban-industrial Mediterranean
1077 city, Marseille (France): Application of the ME-2 solver to inorganic and organic markers, *Atmospheric Research*, 214, 263–
1078 274, <https://doi.org/10.1016/j.atmosres.2018.08.005>, 2018.

1079 Sandradewi, J., Prévôt, A. S. H., Szidat, S., Perron, N., Alfarra, M. R., Lanz, V. A., Weingartner, E., and Baltensperger, U.:
1080 Using Aerosol Light Absorption Measurements for the Quantitative Determination of Wood Burning and Traffic Emission
1081 Contributions to Particulate Matter, *Environ. Sci. Technol.*, 42, 3316–3323, <https://doi.org/10.1021/es702253m>, 2008.

1082 Schmale, J., Shindell, D., von Schneidemesser, E. et al. Air pollution: Clean up our skies. *Nature* 515, 335–337 (2014).
1083 <https://doi.org/10.1038/515335a>

1084 Scerri, M. M., Kandler, K., Weinbruch, S., Yubero, E., Galindo, N., Prati, P., Caponi, L., and Massabò, D.: Estimation of the
1085 contributions of the sources driving PM_{2.5} levels in a Central Mediterranean coastal town, *Chemosphere*, 211, 465–481,
1086 <https://doi.org/10.1016/j.chemosphere.2018.07.104>, 2018.

1087 Simpson, W. R., Brown, S. S., Saiz-Lopez, A., Thornton, J. A., and Von Glasow, R.: Tropospheric Halogen Chemistry:
1088 Sources, Cycling, and Impacts, *Chem. Rev.*, 115, 4035–4062, <https://doi.org/10.1021/cr5006638>, 2015.

1089 Solo-Gabriele, H.: Characteristics of chromated copper arsenate-treated wood ash, *Journal of Hazardous Materials*, 89, 213–
1090 232, [https://doi.org/10.1016/S0304-3894\(01\)00311-9](https://doi.org/10.1016/S0304-3894(01)00311-9), 2002.

1091 Stein, S. E. and Scott, D. R.: Optimization and testing of mass spectral library search algorithms for compound identification,
1092 *J. Am. Soc. Mass Spectrom.*, 5, 859–866, [https://doi.org/10.1016/1044-0305\(94\)87009-8](https://doi.org/10.1016/1044-0305(94)87009-8), 1994.

1093 Su, Y., Wu, D., Li, Q., Ding, X., Chen, Y., Zheng, H., Li, Y., Liu, Y., Liu, A., Wang, S., Cai, R., Wang, L., Jiang, J., Wang,
1094 T., Herrmann, H., George, C., Mellouki, A., and Chen, J.: Multiphase particle formation in industrial plumes corrects missing
1095 sulfate in the urban atmosphere, *One Earth*, 101320, <https://doi.org/10.1016/j.oneear.2025.101320>, 2025.

1096 Sylvestre, A., Mizzi, A., Mathiot, S., Masson, F., Jaffrezo, J. L., Dron, J., Mesbah, B., Wortham, H., and Marchand, N.:
1097 Comprehensive chemical characterization of industrial PM_{2.5} from steel industry activities, *Atmospheric Environment*, 152,
1098 180–190, <https://doi.org/10.1016/j.atmosenv.2016.12.032>, 2017.

1099 Taiwo, A. M., Beddows, D. C. S., Calzolari, G., Harrison, R. M., Lucarelli, F., Nava, S., Shi, Z., Valli, G., and Vecchi, R.:
1100 Receptor modelling of airborne particulate matter in the vicinity of a major steelworks site, *Science of The Total Environment*,
1101 490, 488–500, <https://doi.org/10.1016/j.scitotenv.2014.04.118>, 2014.

1102 Thornton, J. A., Kercher, J. P., Riedel, T. P., Wagner, N. L., Cozic, J., Holloway, J. S., Dubé, W. P., Wolfe, G. M., Quinn, P.
1103 K., Middlebrook, A. M., Alexander, B., and Brown, S. S.: A large atomic chlorine source inferred from mid-continental
1104 reactive nitrogen chemistry, *Nature*, 464, 271–274, <https://doi.org/10.1038/nature08905>, 2010.

1105 Tissari, J., Sippula, O., Torvela, T., Lamberg, H., Leskinen, J., Karhunen, T., Paukkunen, S., Hirvonen, M.-R., and Jokiniemi,
1106 J.: Zinc nanoparticle formation and physicochemical properties in wood combustion – Experiments with zinc-doped pellets in
1107 a small-scale boiler, *Fuel*, 143, 404–413, <https://doi.org/10.1016/j.fuel.2014.11.076>, 2015.

1108 Tobler, A. K., Skiba, A., Wang, D. S., Croteau, P., Styszko, K., Nęcki, J., Baltensperger, U., Slowik, J. G., and Prévôt, A. S.
1109 H.: Improved chloride quantification in quadrupole aerosol chemical speciation monitors (Q-ACSMs), *Atmos. Meas. Tech.*,
1110 13, 5293–5301, <https://doi.org/10.5194/amt-13-5293-2020>, 2020.

1111 Tobler, A. K., Skiba, A., Canonaco, F., Močnik, G., Rai, P., Chen, G., Bartyzel, J., Zimnoch, M., Styszko, K., Nęcki, J., Furger,
1112 M., Róžański, K., Baltensperger, U., Slowik, J. G., and Prevot, A. S. H.: Characterization of non-refractory (NR) PM₁ and
1113 source apportionment of organic aerosol in Kraków, Poland, *Atmos. Chem. Phys.*, 21, 14893–14906,
1114 <https://doi.org/10.5194/acp-21-14893-2021>, 2021.

1115 Tremper, A. H., Font, A., Priestman, M., Hamad, S. H., Chung, T.-C., Pribadi, A., Brown, R. J. C., Goddard, S. L., Grassineau,
1116 N., Petterson, K., Kelly, F. J., and Green, D. C.: Field and laboratory evaluation of a high time resolution x-ray fluorescence
1117 instrument for determining the elemental composition of ambient aerosols, *Atmos. Meas. Tech.*, 11, 3541–3557,
1118 <https://doi.org/10.5194/amt-11-3541-2018>, 2018.

1119 Ulbrich, I. M., Canagaratna, M. R., Zhang, Q., Worsnop, D. R., and Jimenez, J. L.: Interpretation of organic components from
1120 Positive Matrix Factorization of aerosol mass spectrometric data, *Atmospheric Chemistry and Physics*, 9, 2891–2918,
1121 <https://doi.org/10.5194/acp-9-2891-2009>, 2009.

1122 Valavanidis, A., Iliopoulos, N., Gotsis, G., and Fiotakis, K.: Persistent free radicals, heavy metals and PAHs generated in
1123 particulate soot emissions and residue ash from controlled combustion of common types of plastic, *Journal of Hazardous*
1124 *Materials*, 156, 277–284, <https://doi.org/10.1016/j.jhazmat.2007.12.019>, 2008.

1125 Via, M., Chen, G., Canonaco, F., Daellenbach, K. R., Chazeau, B., Chebaicheb, H., Jiang, J., Keernik, H., Lin, C., Marchand,
1126 N., Marin, C., O’Dowd, C., Ovadnevaite, J., Petit, J.-E., Pikridas, M., Riffault, V., Sciare, J., Slowik, J. G., Simon, L.,
1127 Vasilescu, J., Zhang, Y., Favez, O., Prévôt, A. S. H., Alastuey, A., and Cruz Minguillón, M.: Rolling vs. seasonal PMF: real-
1128 world multi-site and synthetic dataset comparison, *Atmos. Meas. Tech.*, 15, 5479–5495, [https://doi.org/10.5194/amt-15-5479-](https://doi.org/10.5194/amt-15-5479-2022)
1129 [2022](https://doi.org/10.5194/amt-15-5479-2022), 2022.

1130 Viana, M., Reche, C., Amato, F., Alastuey, A., Querol, X., Moreno, T., Lucarelli, F., Nava, S., Calzolari, G., Chiari, M., and
1131 Rico, M.: Evidence of biomass burning aerosols in the Barcelona urban environment during winter time, *Atmospheric*
1132 *Environment*, 72, 81–88, <https://doi.org/10.1016/j.atmosenv.2013.02.031>, 2013.

1133 Visser, S., Slowik, J. G., Furger, M., Zotter, P., Bukowiecki, N., Canonaco, F., Flechsig, U., Appel, K., Green, D. C., Tremper,
1134 A. H., Young, D. E., Williams, P. I., Allan, J. D., Coe, H., Williams, L. R., Mohr, C., Xu, L., Ng, N. L., Nemitz, E., Barlow,
1135 J. F., Halios, C. H., Fleming, Z. L., Baltensperger, U., and Prévôt, A. S. H.: Advanced source apportionment of size-resolved
1136 trace elements at multiple sites in London during winter, *Atmos. Chem. Phys.*, 15, 11291–11309, [https://doi.org/10.5194/acp-
1137 15-11291-2015](https://doi.org/10.5194/acp-15-11291-2015), 2015a.

1138 Visser, S., Slowik, J. G., Furger, M., Zotter, P., Bukowiecki, N., Dressler, R., Flechsig, U., Appel, K., Green, D. C., Tremper,
1139 A. H., Young, D. E., Williams, P. I., Allan, J. D., Herndon, S. C., Williams, L. R., Mohr, C., Xu, L., Ng, N. L., Detournay, A.,
1140 Barlow, J. F., Halios, C. H., Fleming, Z. L., Baltensperger, U., and Prévôt, A. S. H.: Kerb and urban increment of highly time-
1141 resolved trace elements in PM₁₀, PM_{2.5} and
1142 PM_{1.0}; winter aerosol in London during ClearfLo 2012, *Atmos. Chem. Phys.*, 15, 2367–2386,
1143 <https://doi.org/10.5194/acp-15-2367-2015>, 2015b.

1144 Wang, H., Wang, X., Yang, X., Li, W., Xue, L., Wang, T., Chen, J., and Wang, W.: Mixed Chloride Aerosols and their
1145 Atmospheric Implications: A Review, *Aerosol Air Qual. Res.*, 17, 878–887, <https://doi.org/10.4209/aaqr.2016.09.0383>, 2017.

1146 Wang, H., Yuan, B., Zheng, E., Zhang, X., Wang, J., Lu, K., Ye, C., Yang, L., Huang, S., Hu, W., Yang, S., Peng, Y., Qi, J.,
1147 Wang, S., He, X., Chen, Y., Li, T., Wang, W., Huangfu, Y., Li, X., Cai, M., Wang, X., and Shao, M.: Formation and impacts
1148 of nitryl chloride in Pearl River Delta, *Atmos. Chem. Phys.*, 22, 14837–14858, <https://doi.org/10.5194/acp-22-14837-2022>,
1149 2022.

1150 Wang, X., Bi, X., Li, H., Zhang, W., Dai, Q., Song, L., Li, L., Wu, J., Zhang, Y., and Feng, Y.: The role of sources and
1151 meteorology in driving PM_{2.5}-bound chlorine, *Journal of Hazardous Materials*, 441, 129910,
1152 <https://doi.org/10.1016/j.jhazmat.2022.129910>, 2023.

1153 Wasson, S. J., Linak, W. P., Gullett, B. K., King, C. J., Touati, A., Huggins, F. E., Chen, Y., Shah, N., and Huffman, G. P.:
1154 Emissions of Chromium, Copper, Arsenic, and PCDDs/Fs from Open Burning of CCA-Treated Wood, *Environ. Sci. Technol.*,
1155 39, 8865–8876, <https://doi.org/10.1021/es050891g>, 2005.

1156 Weber, S., Salameh, D., Albinet, A., Alleman, L. Y., Waked, A., Besombes, J.-L., Jacob, V., Guillaud, G., Meshbah, B., Rocq,
1157 B., Hulin, A., Dominik-Sègue, M., Chrétien, E., Jaffrezo, J.-L., and Favez, O.: Comparison of PM₁₀ Sources Profiles at 15
1158 French Sites Using a Harmonized Constrained Positive Matrix Factorization Approach, *Atmosphere*, 10, 310,
1159 <https://doi.org/10.3390/atmos10060310>, 2019.

1160 Wen, H. and Carignan, J.: Reviews on atmospheric selenium: Emissions, speciation and fate, *Atmospheric Environment*, 41,
1161 7151–7165, <https://doi.org/10.1016/j.atmosenv.2007.07.035>, 2007.

1162 Yu, G., Zhang, Y., Yang, F., He, B., Zhang, C., Zou, Z., Yang, X., Li, N., and Chen, J.: Dynamic Ni/V Ratio in the Ship-
1163 Emitted Particles Driven by Multiphase Fuel Oil Regulations in Coastal China, *Environ. Sci. Technol.*, 55, 15031–15039,
1164 <https://doi.org/10.1021/acs.est.1c02612>, 2021.

1165 Zhuang, H., Chan, C. K., Fang, M., and Wexler, A. S.: Formation of nitrate and non-sea-salt sulfate on coarse particles,
1166 *Atmospheric Environment*, 33, 4223–4233, [https://doi.org/10.1016/S1352-2310\(99\)00186-7](https://doi.org/10.1016/S1352-2310(99)00186-7), 1999.

1167 Zittis, G., Almazroui, M., Alpert, P., Ciais, P., Cramer, W., Dahdal, Y., Fnais, M., Francis, D., Hadjinicolaou, P., Howari, F.,
1168 Jrrar, A., Kaskaoutis, D. G., Kulmala, M., Lazoglou, G., Mihalopoulos, N., Lin, X., Rudich, Y., Sciare, J., Stenchikov, G.,
1169 Xoplaki, E., and Lelieveld, J.: Climate Change and Weather Extremes in the Eastern Mediterranean and Middle East, *Reviews*
1170 *of Geophysics*, 60, e2021RG000762, <https://doi.org/10.1029/2021RG000762>, 2022.

1171